

FEDERAL UNIVERSITY OF SÃO CARLOS  
EXACT SCIENCES AND TECHNOLOGY CENTER  
DEPARTMENT OF CHEMISTRY  
CHEMISTRY POSTGRADUATE PROGRAM

**AMORPHOUS CALCIUM PHOSPHATE NANOPARTICLES  
ALLOW FINGERPRINT DETECTION VIA SELF-  
ACTIVATED LUMINESCENCE**

**Jussara Soares da Silva\***

Thesis presented as part of the requirements to  
obtain the degree of DOCTOR IN SCIENCES,  
concentration area: PHYSICAL CHEMISTRY

**Supervisor: Prof. Dr. Elson Longo**

**\* Scholarship: CNPq (141964/2018-9)**

**São Carlos - SP**

**2022**



## UNIVERSIDADE FEDERAL DE SÃO CARLOS

Centro de Ciências Exatas e de Tecnologia  
Programa de Pós-Graduação em Química

---

### Folha de Aprovação

---

Defesa de Tese de Doutorado da candidata Jussara Soares da Silva, realizada em 20/10/2022.

#### Comissão Julgadora:

Prof. Dr. Elson Longo da Silva (UFSCar)

Prof. Dr. Miguel Ángel San-Miguel Barrera (UNICAMP)

Profa. Dra. Montserrat Español Pons (UPC/Espanha)

Prof. Dr. Juan Manuel Andrés Bort (UJI/Espanha)

Prof. Dr. Ivo Mateus Pinatti (UFMA)

O Relatório de Defesa assinado pelos membros da Comissão Julgadora encontra-se arquivado junto ao Programa de Pós-Graduação em Química.

“The Lord is my shepherd; I shall not want”

Psalm 23:1

## **AGRADECIMENTOS**

*Agradeço imensamente ao Deus todo poderoso por ser meu refúgio! Obrigada Pai, por todos os livramentos que recebi por intermédio de seu filho Jesus Cristo.*

*Gratidão à minha família:*

*aos meu pais, Marlene e Gelson; por seguirem sempre juntos, sendo meu exemplo de vida;*

*aos meus irmãos, Jucinei e Antônio; por sua força e perseverança que me inspiram;*

*aos meus sobrinhos que renovaram minha fé e esperança na pureza e na bondade;*

*e ao Magno; pela paciência durante esses mais de 10 anos de união, por estar comigo.*

*A presença da minha família, com amor, apoio e persistência foi crucial para suportar os momentos difíceis tornando a comemoração de cada pequena vitória mais especial.*

*Grata aos órgãos de fomento, CNPq, FAPESP e CAPES que me auxiliaram financeiramente para a realização deste projeto.*

*Grata aos colegas de pesquisa:*

*ao Prof. Dr. Elson Longo por me aceitar em seu grupo do CDMF como sua orientanda;*

*à Prof<sup>ª</sup>. Dr<sup>ª</sup>. Maria Pau Ginebra por me aceitar em seu grupo de BBT da UPC na Espanha como sua orientanda;*

*ao Prof. Dr. Thales Rafael Machado pela parceria e amizade durante toda a pós graduação;*

*ao Prof. Dr. Maximo Siu Li por todo apoio e gentileza;*

*à Prof<sup>ª</sup>. Dr<sup>ª</sup>. Montserrat Spañol por toda amabilidade e doçura durante meu estágio no exterior;*

*e a todos os companheiros de laboratório, em especial aos doutores Mayara, Andressa, Ivo, Pablo, Francisco e Tiago que me proporcionaram momentos tão divertidos e suaves.*

*Aos não citados, a cada um de vocês que passaram pela minha vida durante esse período, saibam que além da pesquisa, as vivências e trocas de energias, fazem-me ser eternamente grata. Deus os abençoe.*

## FIGURES LIST

- Figure I.** (a) Cores ( $\cap$ ) and deltas ( $\Delta$ ) in fingerprint images belonging to different classes. (b) Examples of fingerprint minutiae: ridge endings ( $\square$ ) and bifurcations (O). (Adapted from Karu *et al.*<sup>8</sup> and Prabhakar *et al.*<sup>9</sup>) ..... 4
- Figure II.** Jablonski diagram of fluorescence and phosphorescence processes and their typical rate constants. (Adapted from Edinburgh Instruments<sup>17</sup>)..... 5
- Figure III.** Schematic illustration of transformation of Posner's clusters to ACP and growth of crystalline HA crystals (Adapted from Roohani *et al.*<sup>28</sup>)..... 7
- Figure 1.** TEM micrographs corresponding to (a) ACP and (b) ACP400 NPs (SAED pattern, inset), (c) EDS elemental analysis of ACP400 NPs, and (d) XRD patterns of prepared samples. .... 18
- Figure 2.** (a) FTIR spectra of ACP and ACP400 samples, (b) magnified view of H<sub>2</sub>O and  $\nu_3\text{CO}_3$  bands, (c,e) magnified views of  $\nu_3/\nu_1\text{PO}_4$  and  $\nu_4\text{PO}_4$  bands, respectively, and (d,f) 2<sup>nd</sup> derivative spectra of  $\nu_3/\nu_1\text{PO}_4$  and  $\nu_4\text{PO}_4$  bands, respectively..... 20
- Figure 3.** (a) Survey XPS spectrum of ACP400 NPs. High-resolution XPS spectra of (b) C 1s and (c) O 1s. .... 23
- Figure 4.**  $E_g$  and  $E_u$  energies for ACP and ACP400 samples. Tauc's plots for (a) direct transition ( $n = 1/2$ ) and (b) indirect transition ( $n = 2$ ). (c) Plots of  $\ln[F(R_\infty)]$  vs. photon energy. .... 24
- Figure 5.** (a,b) PL excitation spectra of ACP and ACP NPs, respectively. PL emission spectra obtained by a (c) spectrofluorometer ( $\lambda_{\text{exc}} = 450$  nm) and (d) HeCd laser ( $\lambda_{\text{exc}} = 442$  nm). (e) Calculated CIE chromaticity coordinates from the PL emission spectra..... 26

<b>Figure 6.</b> PL emission spectra ( $\lambda_{exc} = 405 \text{ nm}$ ) of (a) chemically precipitated HA obtained after ripening for 24 h and after conducting the heat treatment step at 400 °C, (b) PL spectra of ACP and HA heat treated at 400 °C, and (c) normalized PL spectra of ACP and HA heat treated at 400 °C. ....	29
<b>Figure 7.</b> Cell viability analysis of HDFn cells after incubation with increasing concentrations of ACP400 NPs, for 24 and 48 h. Mean $\pm$ SD of three independent experiments in triplicate. Asterisks indicate difference in comparison to the control (*p<0.5 and **p<0.001). ....	32
<b>Figure 8.</b> Latent fingerprint images based on ACP400 NPs obtained under UV irradiation in (a) tweezers and (d) LCD smartphone. (b,e) Digitalized images of UV-exposed surfaces containing ACP400 NPs. (c,f) Digitalized images of the fingerprints obtained from the standard procedure by ink processing. Data analysis was conducted using IAFIS system. ....	33
<b>Figure S1.</b> XRD patterns of (a) HA sample prepared by crystallization of ACP at 24h of reaction time, and (b) HA sample after heat treatment at 400 °C/4h. ....	49
<b>Figure S2.</b> XRD pattern of ACP sample heat treated at 600 °C/4h. ....	49
<b>Figure S3.</b> XRD pattern of ACP400 sample after the thermal aging treatment at 80 °C/8h. ....	50
<b>Figure S4.</b> Magnified view of FTIR spectra on the region corresponding to the $\text{HPO}_4^{2-}$ and $\text{P}_2\text{O}_7^{4-}$ bands.....	50
<b>Figure S5.</b> Diffuse reflectance spectrum of ACP and ACP400 NPs. ....	51
<b>Figure S6.</b> Stability analysis of ACP400 NPs. (a) FTIR, and (b) PL emission spectra. ....	51

## TABLE LIST

<b>Table 1.</b> Phosphate compounds doped with lanthanides as a luminescent material applicable to fingerprint identification.....	6
<b>Table 2.</b> Main calcium orthophosphate compounds (Adapted from Neto <i>et al.</i> <sup>22</sup> ).....	7

## SYMBOLS AND ABBREVIATIONS LIST

A	Proportionality constant
ACP	Amorphous calcium phosphate
ACP400	Sample of ACP heat treated at 400°C for 4h
ATCP	Amorphous tricalcium phosphate
Al-K $\alpha$	K $\alpha$ X-rays of aluminium
a.u.	Arbitrary units
BBT	<i>Biomaterials, Biomecànica i Enginyeria de Teixits</i>
C	Carbon chemical element
Ca-dHA	Calcium-deficient hydroxyapatite
CAP	Calcium orthophosphate
CAPES	<i>Coordenação de Aperfeiçoamento de Pessoal de Nível Superior</i>
Ca(NO <sub>3</sub> ) <sub>2</sub> ·4H <sub>2</sub> O	Calcium nitrate tetrahydrate
Ca <sub>3</sub> (PO <sub>4</sub> ) <sub>2</sub>	Amorphous tricalcium phosphate
Ca <sub>9</sub> (PO <sub>4</sub> ) <sub>6</sub>	Calcium phosphate clusters
Ca <sup>2+</sup>	Calcium ion
CB	Conduction band
CDMF	<i>Centro de Desenvolvimento de Materiais Funcionais</i>
CIE	<i>Comission Internationale de l'Éclairage</i>
CNPq	<i>Conselho Nacional de Desenvolvimento Científico e Tecnológico</i>
CO <sub>2</sub>	Carbon dioxide
CO <sub>3</sub> <sup>2-</sup>	Carbonate groups
CO <sub>2</sub> <sup>•-</sup>	Carbon dioxide radical anion
Cu K $\alpha$	K $\alpha$ X-rays of copper
DFT	Density functional theory
DNA	Deoxyribonucleic acid
DMEM	Dulbecco's modified eagle's medium
DMSO	Dimethyl sulfoxide



EDS	Energy-dispersive X-ray Spectroscopy
$E_a$	Activation energy
$E_g$	Band gap energy
$E_u$	Urbach energy
eV	Electron-volt
FAPESP	<i>Fundação de Amparo à Pesquisa do Estado de São Paulo</i>
FBI	Federal bureau of investigation
FBS	Fetal bovine serum
FTIR	Fourier transform infrared spectroscopy
FWHM	Full width at half maximum
GNANO	<i>Grupo de Nanomedicina e Nanotoxicologia</i>
h	Hour
$H_L$	Left components
$H_R$	Right components
HA	Hydroxyapatite
HA400	Sample of HA heat treated at 400°C for 4h
HDFn	Human dermal fibroblast neonatal
HeCd laser	Helium-cadmium laser
$\text{HPO}_4^{2-}$	Acidic phosphate groups
$h\nu$	Incident photon energy
$\text{H}_2\text{O}$	Water molecule
IAFIS	Integrated automated fingerprint identification system
ICSD	Inorganic Crystal Structure Data
ISC	Intersystem crossing
INAMAT <sup>2</sup>	Institute for Advanced Materials and Mathematics
kV	Kilovolts or $10^3$ volts
LCD	Liquid Crystal Display
ln	Natural logarithm

LRO	Long-range ordering
mg/mL	Miligram per milliliter or $10^{-3}$ m/ $10^{-3}$ L
meV	Milielelectronvolts or $10^{-3}$ eV
min	Minute
mmol	Milimol or $10^{-3}$ mol
MTT	3-[4,5-dimethylthiazol-2-yl]-2,5-diphenyltetrazolium bromide
nm	Nanometer or $10^{-9}$ m
NMR	Nuclear magnetic resonance spectroscopy
(NH <sub>4</sub> ) <sub>2</sub> HPO <sub>4</sub>	Di-ammonium phosphate
NPs	Nanoparticles
NUV	Near-ultraviolet
O	Oxygen chemical element
OH	Hydroxyl groups
P	Phosphorus chemical element
pH	Potential of hydrogen
PL	Photoluminescence or photoluminescent
PO <sub>4</sub> <sup>3-</sup>	Phosphate groups
P <sub>2</sub> O <sub>7</sub> <sup>4-</sup>	Pyrophosphate ion
QDs	Quantum dots
R <sub>∞</sub>	Reflectance
<i>s</i>	Scattering coefficient
SAED	Selected area electron diffraction
SCAI	<i>Servicios Centrales de Apoyo a la Investigación</i>
SD	Standard deviation
SRO	Short-range ordering
TEM	Transmission electron microscopy
UFSCar	<i>Universidade Federal de São Carlos</i>
UPC	<i>Universitat Politècnica de Catalunya</i>

UV	Ultraviolet
UV-Vis	Ultraviolet-visible spectroscopy
VB	Valence band
V <sub>Ca</sub>	Calcium vacancies
V <sub>H</sub>	Hydrogen vacancies
V <sub>O</sub>	Oxygen vacancies
V <sub>OH</sub>	Hydroxyl vacancies
v/v	Volume/volume percentage
W	Watt
wt%	Weight percent
Xe lamp	Xenon lamp
XPS	X-ray photoelectron spectroscopy
XRD	X-ray diffraction
ZnS	Zinc sulfide phosphor
$\alpha$	Absorption coefficient
$\alpha$ -TCP	Alpha-tricalcium phosphate
$\beta$ -TCP	Beta-tricalcium phosphate
$\Delta S$	Peak asymmetry
$\lambda$	Wavelength
$\lambda_{exc}$	Excitation wavelength
$\lambda_{em}$	Emission wavelength
$\mu L$	Microliter or $10^{-6}$ L
$\mu m$	Micrometer or $10^{-6}$ m
$\mu g/mL$	Microgram per milliliter or $10^{-6}$ g/ $10^{-3}$ L
$\nu_1$	Symmetric stretching mode
$\nu_2$	Bending mode
$\nu_3$	Asymmetric stretching mode
$\nu_4$	Bending mode

$\text{\AA}$	Angstrom
$^{\circ}\text{C}$	Degrees Celsius
$1s$	Electronic Distribution Sub-Level
$1/n$	Informs the type of transition
$2p$	Electronic Distribution Sub-Level
$2s$	Electronic Distribution Sub-Level
$2\theta$	Degrees 2 theta
$3p$	Electronic Distribution Sub-Level
$3s$	Electronic Distribution Sub-Level
$3d$	Electronic Distribution Sub-Level
$4s$	Electronic Distribution Sub-Level

## **RESUMO**

*DETECÇÃO DE IMPRESSÕES DIGITAIS POR MEIO DA LUMINESCÊNCIA AUTOATIVADA DE NANOPARTÍCULAS DE FOSFATO DE CÁLCIO AMORFO.* Neste trabalho, foram obtidas pela primeira vez nanopartículas fotoluminescentes estáveis sem ativadores, baseadas em fosfato de cálcio amorfo (ACP); e seu desempenho para imagens de impressões digitais latentes foi investigado. Nanopartículas de ACP com formato arredondado irregular e diâmetros na faixa de 10–40 nm foram preparadas por precipitação química rápida e simples, seguida de tratamento térmico a 400 °C por 4 h. As espectroscopias de refletância difusa e fotoluminescência, tanto emissão quanto excitação, revelam uma alta densidade de estados de energia localizados dentro do amplo intervalo de banda óptica do ACP tratado termicamente (por exemplo, 5,25–5,42 eV). Este comportamento permitiu a excitação do ACP na região do ultravioleta (UV) próximo ( $\lambda_{exc}=450$  nm, 2,75 eV), levando a uma intensa emissão de fotoluminescência de banda larga relacionada a defeitos (490-890 nm) centrada em 540 nm (2,30 eV), 50 vezes mais intensa do que nanopartículas não tratadas. O efeito de retração da rede (devido à eliminação de água estrutural), a presença de vacâncias iônicas ( $V_{Ca}$  e  $V_O$  em  $PO_4^{3-}$ ) e grupos carbonato ( $CO_3^{2-}$ ), foram discutidos em detalhes, tanto nas propriedades luminescentes do ACP, quanto após a cristalização em meio aquoso do ACP à hidroxiapatita (HA). As nanopartículas de ACP apresentaram acitotoxicidade, conforme determinado pelo ensaio MTT em linhagem celular Neonatal de Fibroblasto Dérmico Humano (HDFn), com viabilidade celular superior a 95% em todas as concentrações testadas (20–320  $\mu\text{g/mL}$ ), após incubação por 24 e 48 h. As imagens latentes da impressão digital foram obtidas usando as nanopartículas ACP sob radiação UV próximo ( $\lambda_{exc} = 450$  nm) em pinças e tela de smartphone LCD, validadas com sucesso pelo Sistema Integrado de Identificação Automatizada de Impressões Digitais usado pela Polícia Científica na Espanha. Os LRO presentes resultados evidenciaram que as novas nanopartículas luminescentes de ACP são seguras para serem usadas e estão de acordo com os requisitos forenses para futuras ações judiciais.

**Palavras-chave:** Fosfato de cálcio. Nanopartículas. Luminescência. Defeitos. Forense. Imagem de impressão digital

## ABSTRACT

AMORPHOUS CALCIUM PHOSPHATE NANOPARTICLES ALLOW FINGERPRINT DETECTION VIA SELF-ACTIVATED LUMINESCENCE. In this work, stable activator-free photoluminescent nanoparticles based on amorphous calcium phosphate (ACP) were obtained for the first time, and their performance for latent fingerprint imaging was investigated. ACP nanoparticles with irregular rounded shape and diameters in 10–40 nm range were prepared by a rapid and simple chemical precipitation followed by heat treatment at 400 °C for 4 h. Notably, diffuse reflectance spectroscopy, photoluminescence excitation and emission measurements reveal a high density of localized energy states within the wide optical band gap of heat-treated ACP ( $E_g = 5.25\text{--}5.42$  eV). This behavior allowed the excitation of ACP in near-ultraviolet region ( $\lambda_{\text{exc}} = 450$  nm, 2.75 eV), leading to an intense defect-related broadband (490–890 nm) photoluminescence emission centered at 540 nm (2.30 eV), 50 times more intense than untreated nanoparticles. The effect of lattice shrinkage due to structural water elimination, the presence of ionic vacancies ( $V_{\text{Ca}}$  and  $V_{\text{O}}$  in  $PO_4^{3-}$ ) and carbonate groups ( $CO_3^{2-}$ ), on the luminescent properties of ACP were discussed in detail, as well as investigated after aqueous-mediated ACP crystallization into hydroxyapatite (HA). ACP nanoparticles were non-cytotoxic, as determined by MTT assay in Human Dermal Fibroblast neonatal (HDFn) cell line, with cell viabilities superior to 95% in all tested concentrations (20–320  $\mu\text{g/mL}$ ), after incubation for 24 and 48 h. Latent fingerprint images were obtained using the ACP nanoparticles under near-ultraviolet irradiation ( $\lambda_{\text{exc}} = 450$  nm) in tweezers and LCD smartphone and successfully validated by the Integrated Automated Fingerprint Identification System used by Scientific Police in Spain. The present results evidenced that the new luminescent ACP nanoparticles are safe to be used and agree with the forensic requirements for future legal actions.

**Keywords:** Calcium phosphate. Nanoparticles. Luminescence. Defects. Forensics. Fingerprint imaging

## TABLE OF CONTENTS

1	– PUBLICATIONS .....	1
1.1	– Thesis Publication .....	1
1.2	– Other Publications .....	1
1.3	– More Information .....	1
2	– INTRODUCTION .....	3
3	– GOALS .....	9
3.1	– Specific goals.....	9
4	– IS IT POSSIBLE TO OBTAIN ENHANCED LUMINESCENCE OF CALCIUM ORTHOPHOSPHATES WITHOUT ADDITION OTHER ELEMENTS? .....	10
4.1	Abstract.....	12
4.2	Introduction.....	13
4.3	Materials and methods .....	14
4.4	Results and discussion .....	17
4.5	Conclusions.....	34
4.6	Acknowledgments .....	34
4.7	References.....	35
4.8	Supplementary material.....	48
5	– CONCLUSIONS .....	52
6	– REFERENCES .....	53

# 1 – PUBLICATIONS

## 1.1 – Thesis Publication

1 - Machado, T. R.; **Da Silva, J. S.**; Miranda, R. R.; Zucolotto, V; Li, M. S.; Yuso, M. V. M.; Guerrero-González, J. J.; Rosa, I. L. V.; Algarra, M.; Longo, E. Amorphous calcium phosphate nanoparticles allow fingerprint detection via self-activated luminescence. CHEMICAL ENGINEERING JOURNAL, v. 443, p. 136443, 2022.

DOI: 10.1016/j.cej.2022.136443

## 1.2 – Other Publications

2 - Machado, T.R.; **Da Silva, J. S.**; Cordoncillo, E.; Beltrán-Mir, H.; Andrés, J.; Zucolotto, V; Longo. Advances in the Synthesis and Applications of Self-Activated Fluorescent Nano- and Micro-Hydroxyapatite. In: Taft, C.A., de Lazaro, S.R. (eds) Research Topics in Bioactivity, Environment and Energy. Engineering Materials. SPRINGER, CHAM. p. 149–18, 2022. DOI: 10.1007/978-3-031-07622-0\_5

3 - Assis, M.; **Da Silva, J.S.**; Gonçalves, M.O.; Rodolpho, J.M.A.; Fragelli, B.D.L.; Corte, A.B.P.; Ribeiro, L.K.; Teodoro, M.D.; Anibal, F.F.; Sousa, C.P.; Oliveira Jr., O.N.; Andrés, J.; Longo, E. Bactericidal activity of  $\text{Ag}_4\text{V}_2\text{O}_7/\beta\text{-AgVO}_3$  heterostructures against antibiotic-resistant *Klebsiella pneumoniae*. BIOMATERIALS ADVANCES, v. 141, p. 213097, 2022. DOI: 10.1016/j.bioadv.2022.213097

4 - Teixeira, M. M.; Santos, L. C.; Tello, A. C. M.; Almeida, P. B.; **Da Silva, J. S.**; Laier, L.; Gracia, L.; Teodoro, M. D.; da Silva, L. F.; Andres, J.; Longo, E.  $\alpha\text{-Ag}_2\text{WO}_4$  under microwave, electron beam and femtosecond laser irradiations: Unveiling the relationship between morphology and photoluminescence emissions. JOURNAL OF ALLOYS AND COMPOUNDS, v. 903, p. 163840, 2022. DOI: 10.1016/j.jallcom.2022.163840

5 - **Da Silva, J. S.**; Machado, T. R.; Trench, A. B.; Silva, A. D; Teodoro, V.; Vieira, P. C.; Martins, T. A.; Longo, E. Enhanced photocatalytic and antifungal activity of hydroxyapatite/ $\alpha\text{-AgVO}_3$  composites. MATERIALS CHEMISTRY AND PHYSICS, v. 252, p. 123294, 2020. DOI: 10.1016/j.matchemphys.2020.123294



6 - Machado, T. R.; Leite, I. S.; Inada, N. M.; Li, M. S.; **Da Silva, J. S.**; Andrés, J.; Beltrán-Mir, H.; Cordoncillo, E.; Longo, E. Designing biocompatible and multicolor fluorescent hydroxyapatite nanoparticles for cell-imaging applications. *MATERIALS TODAY CHEMISTRY*, v 14, p. 100211, 2019. DOI:10.1016/j.mtchem.2019.100211

7 - **Da Silva, J. S.**; Machado, T. R.; Martins, T. A.; Assis, M.; Foggi, C. C.; Macedo, N. G.; Beltrán-Mir, H.; Cordoncillo, Andres, J.; Longo, E.  $\alpha$ -AgVO<sub>3</sub> Decorated by Hydroxyapatite (Ca<sub>10</sub>(PO<sub>4</sub>)<sub>6</sub>(OH)<sub>2</sub>): Tuning Its Photoluminescence Emissions and Bactericidal Activity. *INORGANIC CHEMISTRY*, v. 58, p. 5900–5913, 2019. DOI: 10.1021/acs.inorgchem.9b00249

8 - Oliveira, R. C.; Teixeira, M. M.; Costa, J. P. C.; Penha, M.; Francisco, E. M.; **Da Silva, J. S.**; Li, M. S.; Longo, E.; Gracia, L.; Andrés, J.  $\alpha$ - and  $\beta$ -AgVO<sub>3</sub> polymorphs as photoluminescent materials: An example of temperature-driven synthesis. *CERAMICS INTERNATIONAL*, v. 44(6), p. 5939–5944, 2018. DOI:10.1016/j.ceramint.2017.12.161

### 1.3 More information:



<https://www.linkedin.com/in/jussara-s-038b29120/>



<http://lattes.cnpq.br/2586454534909121>

## 2 – INTRODUCTION

Fingerprints for identification are of extreme importance to society, useful to data control, to link a series of crimes and to identify victims after natural or man-made disasters such as an earthquake or bombing <sup>1</sup>. Of the biometric techniques, fingerprint identification is more commonly used and effective even after the advent of DNA, since Latent fingerprints are found at crime scenes much more commonly than are body fluids that contain DNA <sup>2</sup>.

The use of fingerprints for identification purposes began nearly 100 years ago with the ink pad and Henry classification system, but at the end of the 19th century when the Federal Bureau of Investigation (FBI) developed the Integrated Automated Fingerprint Identification System (IAFIS) that occurred the true revolution in this sector <sup>3-5</sup>.

The software does complex and accurate processes based on mathematical algorithms that evaluate several features of fingerprints. Starts with a filtration comparing the scars, pores, creases, warts, whorl's direction, the construction of cores and triangles as well as positions of the same (**Figure Ia**), on the fingerprints obtained at the crime scene with fingerprints of database printed on paper or equipment. Only those that best match these critical characteristics proceed to the next step which is “resource matching”, i.e., to mark the corresponding minutiae (**Figure Ib**) <sup>6-10</sup>.

But for this process to be successful, a good gathering of fingerprints at the crime scene must be ensured, with high sharpness, contrast, and size <sup>11</sup>. However, only patent fingerprints and plastic fingerprints are easily seen by the human eye. Patent fingerprints can be made with blood, grease, ink or dirt; and plastic fingerprints are three-dimensional prints and can be made by pressing your fingers into fresh ink, wax, soap, or even candy <sup>7, 10, 12</sup>.

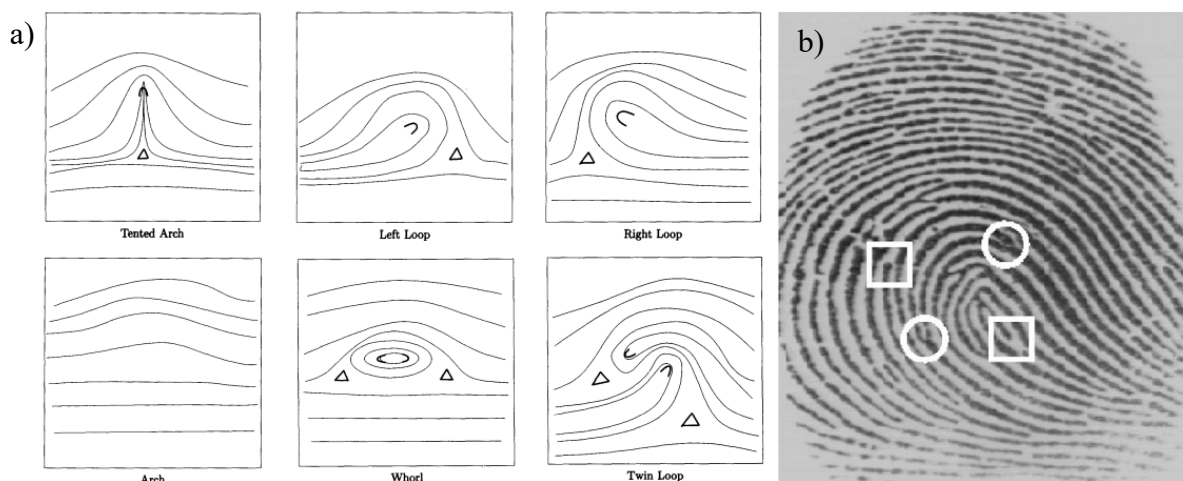


**Figure I. (a)** Cores ( $\cap$ ) and deltas ( $\Delta$ ) in fingerprint images belonging to different classes. **(b)** Examples of fingerprint minutiae: ridge endings ( $\square$ ) and bifurcations ( $\circ$ ). (Adapted from Karu *et al.*<sup>8</sup> and Prabhakar *et al.*<sup>9</sup>)

In turn, latent fingerprints are either barely visible or invisible to the naked eye. The complex emulsion of water, amino acids, proteins, urea, lactic acid, sugars released by the fingers added to fatty compounds, and oils from contamination through touching other parts of the body such as the forehead, hair, and neck; form these fingerprints. Therefore, additional processing is required for latent prints to be seen with the use of materials called revealers<sup>7, 10, 12–14</sup>.

Generally, techniques with fingerprint revealers powders type most used at crime scenes, due to their ease of use and because some objects cannot be taken to a laboratory<sup>10, 12, 14</sup>. The fingerprint dusting formulations may be broadly classified into three types: regular (a resinous polymer for adhesion and a colorant for contrast), metallic (usually toxic powder metals), and luminescent (powders that emit light by stimulus)<sup>10, 13–15</sup>. In this work, we developed a powder that fits this last description, specifically, a photoluminescent powder.

It is known that the term luminescence is a general term for the process of releasing energy in the form of light and different names for this process can be assigned accordingly to the source used for the excitation of the material. In this sense, electroluminescence occurs through excitation with electrical energy; chemiluminescence through the energy of chemical reactions; and so on<sup>16, 17</sup>.

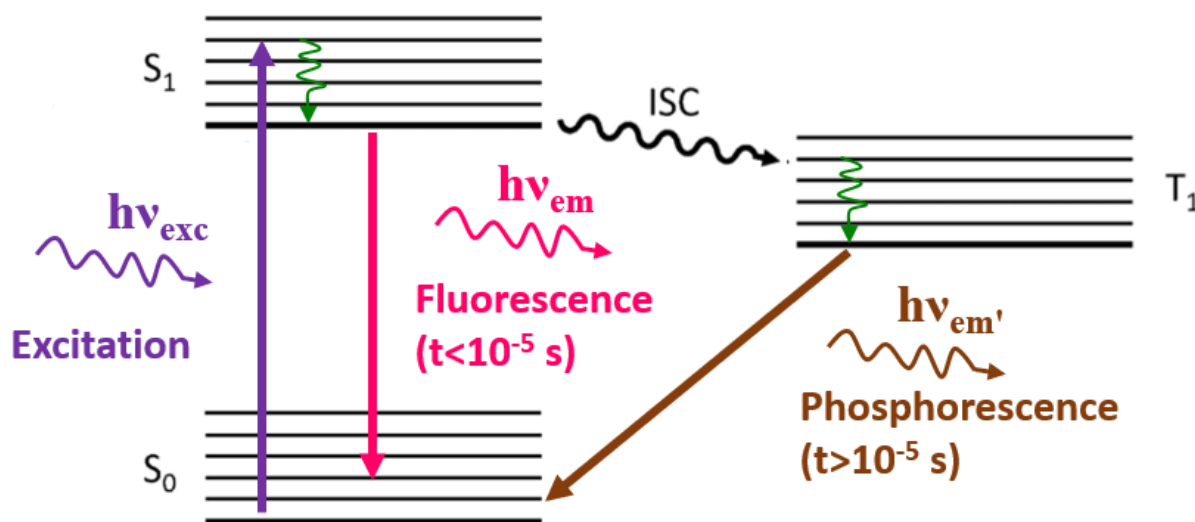


**Figure II.** Jablonski diagram of fluorescence and phosphorescence processes and their typical rate constants. (Adapted from Edinburgh Instruments <sup>17</sup>)

Photoluminescence (PL) follows the same reasoning, and light is the energy source. When matter absorbs photons, the electrons move from the lower energy level (ground state) to the higher energy level (excited state). Then the electrons return to the ground state, releasing the excess energy in the form of visible electromagnetic radiation. This can occur in two different ways, by fluorescence with instant emission, short times lesser than  $10^{-5}$  s; or by phosphorescence that has a transition between two electronic states with different spin multiplicities, entailing delayed emission i.e., long times over than  $10^{-5}$  s (**Figure II**) <sup>16,17</sup>.

In this context, fingerprint revealing is commonly achieved with fluorescent organic compounds, but they are not efficient for detecting fingerprints on porous or reflective surfaces. Inorganic phosphors are a good solution as they have variable color emission characteristics, residual gloss, high chemical stability, and nano-size, which allow fingerprint detection on any porous or non-porous surfaces <sup>11</sup>. Publications about nanoparticles as new latent fingerprint developers have increased in the last decade. However, despite a large number of studies in this context, few are actually used in forensic routines due to the lack of details about their interaction with fingerprint components and the toxicity of some components <sup>13</sup>. Generally, phosphate-based luminescent materials present emissions applicable to latent fingerprint identification when doped with lanthanides (**Table 1**) <sup>18-21</sup>.

**Table 1.** Phosphate compounds doped with lanthanides as a luminescent material applicable to fingerprint identification.

Composition	$\lambda_{exc}$ (nm)	Surface where was applied	Reference
La(PO <sub>4</sub> ):Ce, Tb	254	Aluminum alloys sheets, ceramic tiles, marbles, painted wood, printing papers, and wood floor	Wang <i>et al.</i> , 2015 <sup>18</sup>
Sr <sub>10</sub> (PO <sub>4</sub> ) <sub>6</sub> O:Ce <sup>3+</sup>	254	Aluminum foil, stainless steel, glass, compact disk, credit card	Park <i>et al.</i> , 2018 <sup>19</sup>
Ca <sub>4</sub> (PO <sub>4</sub> ) <sub>2</sub> O:Eu <sup>2+</sup>	395	Slide glass, stainless steel, polystyrene dish, and plastic banknotes.	Hong <i>et al.</i> , 2018 <sup>20</sup>
Gd <sub>0.95</sub> Eu <sub>0.05</sub> PO <sub>4</sub>	395	Petri dish, compact stainless steel, aluminum foil, transparent glass slide, amber glass, disc, black marble, green leaf	Pushendra <i>et al.</i> , 2022 <sup>21</sup>

Different nanoparticles make up the calcium orthophosphate (CaP) family (**Table 2**) and all are widely known for their non-toxicity<sup>16, 22</sup>. Particular emphasis is given to the investigation of the luminescence of hydroxyapatite (HA), due to interest in biomedical applications, but only during the 2000s, studies were started on the autoluminescence of HA, that is, without the addition of extra components<sup>23, 24</sup>. Years later, researchers investigated intrinsic PL, obtaining it through controlled synthesis followed by heat treatments. This phenomenon was possible because HA has an extremely flexible structure susceptible to a wide range of structural defects (distortions, ionic vacancies, impurities) that can be optimized to produce intrinsic PL<sup>16, 25, 26</sup>.

The synthesis of CaP is full of nuances, and highly dependent on the prevailing physicochemical conditions, mainly the synthesis time, Ca and PO<sub>4</sub> concentration, pH, and temperature. For example, it is known that amorphous calcium phosphate is a thermodynamically stable hydroxyapatite precursor phase, as illustrated in **Figure III**<sup>16, 27–30</sup>.

**Table 2.** Main calcium orthophosphate compounds (Adapted from Neto *et al.* <sup>22</sup>)

Compound	Formula	Ca/P	Symbol
Monocalcium phosphate anhydrous	$\text{Ca}(\text{H}_2\text{PO}_4)_2$	0.50	MCPA
Monocalcium phosphate monohydrate	$\text{Ca}(\text{H}_2\text{PO}_4)_2 \cdot 2\text{H}_2\text{O}$	0.50	MCPM
Dicalcium phosphate anhydrous	$\text{CaHPO}_4$	1.00	DCPA
Dicalcium phosphate dihydrate	$\text{CaHPO}_4 \cdot 2\text{H}_2\text{O}$	1.00	DCPD
Octacalcium phosphate	$\text{Ca}_8\text{H}_2(\text{PO}_4)_6 \cdot 5\text{H}_2\text{O}$	1.33	OCP
Amorphous calcium phosphate <sup>1</sup>	$\text{Ca}_x\text{H}_y(\text{PO}_4)_z \cdot n\text{H}_2\text{O}$	0.67-1.67	ACP
$\alpha$ -Tricalcium phosphate	$\alpha\text{-Ca}_3(\text{PO}_4)_2$	1.50	$\alpha$ -TCP
$\beta$ -Tricalcium phosphate	$\beta\text{-Ca}_3(\text{PO}_4)_2$	1.50	$\beta$ -TCP
Calcium-deficient hydroxyapatite <sup>2</sup>	$\text{Ca}_{10-x}(\text{HPO}_4)_x(\text{PO}_4)_{6-x}(\text{OH})_{2-x}$	1.5-1.67	Ca-dHA
Sintered hydroxyapatite	$\text{Ca}_{10}(\text{PO}_4)_6(\text{OH})_2$	1.67	HA
Tetracalcium phosphate	$\text{Ca}_4(\text{PO}_4)_2\text{O}$	2.00	TTCP

<sup>1</sup> The ACP normally has  $x = 3$ ,  $y = 3$ ,  $z = 2$ , and  $n = 3-4.5$ ; 15–20%  $\text{H}_2\text{O}$ .

<sup>2</sup>  $x$  may vary between 0 and 1. When  $x = 1$  (the boundary condition with  $\text{Ca/P} = 1.5$ )

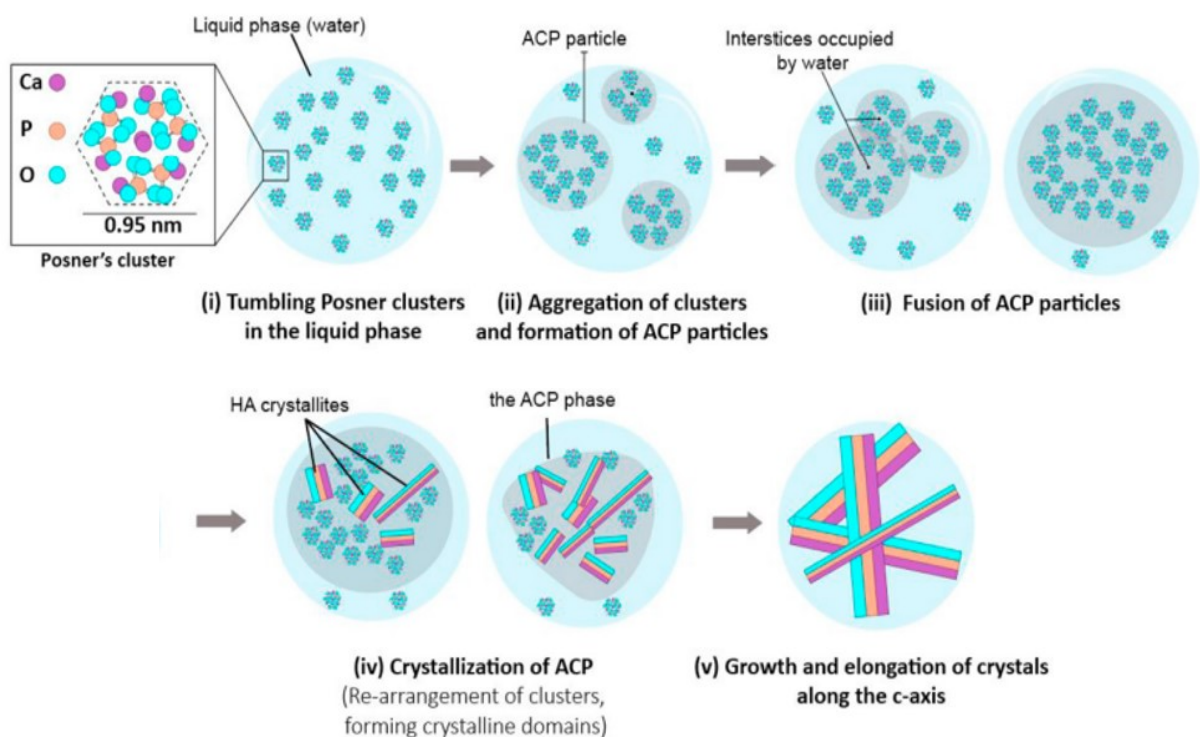


**Figure III.** Schematic illustration of transformation of Posner's clusters to ACP and growth of crystalline HA crystals (Adapted from Roohani *et al.* <sup>28</sup>)

A long-range ordered material has a high periodicity of the three-dimensional lattice having a greater crystalline character. On the other hand, when there is a periodicity deficit, the material is less ordered at the long-range and the amorphous character of the material is more relevant <sup>16,26</sup>. In this way, has possible to switch from one structure to another by short- and long-range ordering of the species that form the structure of the material, that's why the ACP is a precursor to several other CAPs.

Therefore, the objective of the present work was to obtain stable and non-toxic ACP through a simple and fast synthesis in order to improve its luminescent properties as well as to understand the influence of structural changes in short- and long-range in this process. Finally, to verify the feasibility of applying this material as latent fingerprint revealers, through world-reliable forensic systems.

### **3 – GOALS**

The overall objective consists of obtaining calcium orthophosphates (CAP) and treating them to improve their properties, analyzing their characteristics and making them applicable to society.

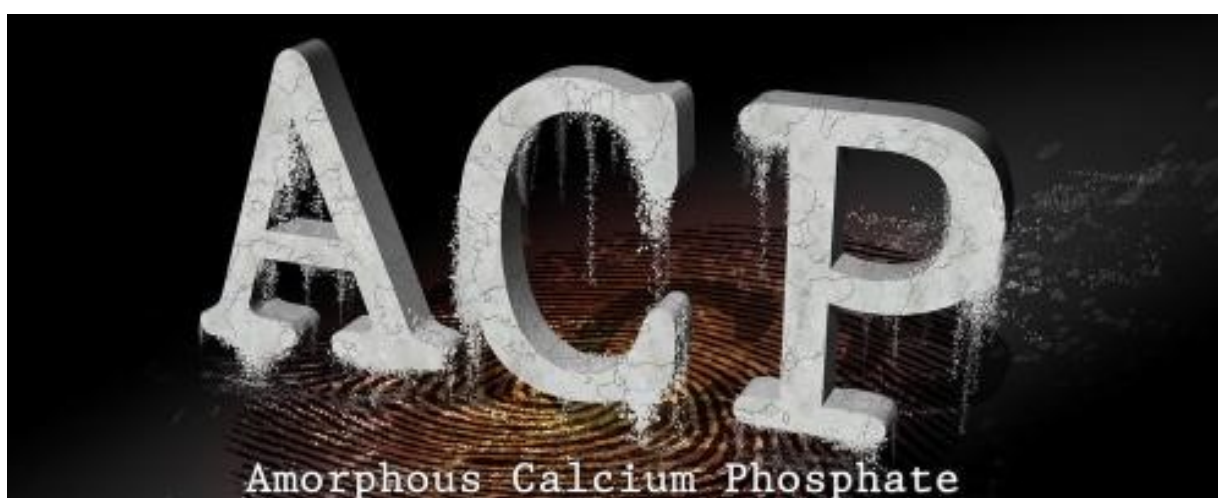
#### **3.1 – Specific goals**

- Synthesize calcium-deficient hydroxyapatite (Cad-HA);
- Synthesize amorphous calcium phosphate (ACP);
- Perform thermal treatments in these CAPS;
- Characterize the materials obtained as regards morphology, long-range ordering (LRO), short-range ordering (SRO), optical properties, surface, cytotoxicity, and photoluminescence (PL) properties.
- To apply the CAP with self-luminescence improved as a latent fingerprint revealers powder.



## 4 – IS IT POSSIBLE TO OBTAIN ENHANCED LUMINESCENCE OF CALCIUM ORTHOPHOSPHATES WITHOUT ADDITION OTHER ELEMENTS?

The contents of this section are the results of studies developed during the doctorate, which enabled the elaboration of the article entitled “Amorphous Calcium Phosphate Nanoparticles Allow Fingerprint Detection via Self-Activated Luminescence”, made in collaboration with Brazilian and Spanish researchers, used as the base publication of this thesis as follows on the next pages.



Chemical Engineering Journal 443 (2022) 136443



Contents lists available at ScienceDirect

Chemical Engineering Journal

journal homepage: [www.elsevier.com/locate/cej](http://www.elsevier.com/locate/cej)



<https://doi.org/10.1016/j.cej.2022.136443>



Amorphous calcium phosphate nanoparticles allow fingerprint detection via self-activated luminescence

Thales R. Machado<sup>a,b,\*</sup>, Jussara S. da Silva<sup>b</sup>, Renata R. Miranda<sup>a</sup>, Valtencir Zucolotto<sup>a</sup>, Máximo S. Li<sup>c</sup>, M. Valle Martínez de Yuso<sup>d</sup>, Juan J. Guerrero-González<sup>e</sup>, Ieda L.V. Rosa<sup>b</sup>, Manuel Algarra<sup>f,\*</sup>, Elson Longo<sup>b</sup>

<sup>a</sup> GNANO - Nanomedicine and Nanotoxicology Group, Physics Institute of São Carlos, University of São Paulo, 13566-590 São Carlos, SP, Brazil

<sup>b</sup> CDMF - Center for the Development of Functional Materials, Federal University of São Carlos, 13565-905 São Carlos, SP, Brazil

<sup>c</sup> Physics Institute of São Carlos, University of São Paulo, São Carlos, SP, Brazil

<sup>d</sup> X-Ray Photoelectron Spectroscopy Lab, Central Service to Support Research Building (SCAI), University of Málaga, 29071 Málaga, Spain

<sup>e</sup> Policía Científica, Cuerpo Nacional de Policía, Málaga, Spain

<sup>f</sup> INAMAT<sup>2</sup>-Institute for Advanced Materials and Mathematics, Public University of Navarre, Campus de Arrosadía, 31006 Pamplona, Spain



# Amorphous Calcium Phosphate Nanoparticles Allow Fingerprint Detection via Self-Activated Luminescence

Thales R. Machado,<sup>a,b,\*</sup> Jussara S. da Silva,<sup>b</sup> Renata R. Miranda,<sup>a</sup> Valtencir Zucolotto,<sup>a</sup> Máximo S. Li,<sup>c</sup> Maria V.M. de Yuso,<sup>d</sup> Juan J. Guerrero-González,<sup>e</sup> Ieda L.V. Rosa,<sup>b</sup> Manuel Algarra,<sup>f,g,\*</sup> Elson Longo<sup>b</sup>

<sup>a</sup> GNANO - Nanomedicine and Nanotoxicology Group, Physics Institute of São Carlos, University of São Paulo, 13566-590 São Carlos, SP, Brazil.

<sup>b</sup> CDMF - Center for the Development of Functional Materials, Federal University of São Carlos, 13565-905 São Carlos, SP, Brazil.

<sup>c</sup> IFSC - Physics Institute of São Carlos, University of São Paulo, São Carlos, SP, Brazil.

<sup>d</sup> SCAI - Central Service to Support Research Building (X-Ray Photoelectron Spectroscopy Lab.), University of Málaga. 29071 Málaga, Spain

<sup>e</sup> Policía Científica, Cuerpo Nacional de Policía, Málaga, Spain.

<sup>f</sup> Departamento de Ciencias, Universidad Pública de Navarra, Campus de Arrosadia, 31006 Pamplona, Spain.

<sup>g</sup> INAMAT<sup>2</sup>-Institute for Advanced Materials and Mathematics, Campus de Arrosadia 31006 Pamplona, Spain.

## 4.1. Abstract

Herein, stable activator-free photoluminescent nanoparticles based on amorphous calcium phosphate (ACP) were obtained for the first time, and their performance for latent fingerprint imaging was investigated. ACP nanoparticles with irregular rounded shape and diameters in 10–40 nm range were prepared by a rapid and simple chemical precipitation followed by heat treatment at 400 °C for 4 h. Notably, diffuse reflectance spectroscopy, photoluminescence excitation and emission measurements reveal a high density of localized energy states within the wide optical band gap of heat-treated ACP ( $E_g = 5.25\text{--}5.42$  eV). This behavior allowed the excitation of ACP in near-ultraviolet region ( $\lambda_{\text{exc}} = 450$  nm, 2.75 eV), leading to an intense defect-related broadband (490–890 nm) photoluminescence emission centered at 540 nm (2.30 eV), 50 times more intense than untreated nanoparticles. The effect of lattice shrinkage due to structural water elimination, the presence of ionic vacancies ( $V_{\text{Ca}}$  and  $V_{\text{O}}$  in  $PO_4^{3-}$ ) and carbonate groups ( $CO_3^{2-}$ ), on the luminescent properties of ACP were discussed in detail, as well as investigated after aqueous-mediated ACP crystallization into hydroxyapatite (HA). ACP nanoparticles were non-cytotoxic, as determined by MTT assay in Human Dermal Fibroblast neonatal (HDFn) cell line, with cell viabilities superior to 95% in all tested concentrations (20–320  $\mu\text{g/mL}$ ), after incubation for 24 and 48 h. Latent fingerprint images were obtained using the ACP nanoparticles under near-ultraviolet irradiation ( $\lambda_{\text{exc}} = 450$  nm) in tweezers and LCD smartphone and successfully validated by the Integrated Automated Fingerprint Identification System used by Scientific Police in Spain. The present results evidenced that the new luminescent ACP nanoparticles are safe to be used and agree with the forensic requirements for future legal actions.

## 4.2. Introduction

Fingerprint analysis is one of the most explored biometric recognition approaches in forensic science for personal identification [1,2]. Usually, fingerprints left on surfaces cannot be observed by naked eyes, and a post processing step is often necessary, such as powder dusting, chemical fuming, and through typical formulations based on organic and fluorescent dyes [3–8]. Remarkably, since the pioneer use of zinc sulfide phosphor (ZnS) [9], the photoluminescent powders have been the most requested approach due to their resistance to photobleaching, and the ability to produce high resolution and sensitive fingermarks when illuminated under ultraviolet (UV) radiation.

Up to now, a variety of strategies based on nanotechnology have been developed to obtain fluorescent images of fingerprints with higher contrast by the improvement of the fluorescence intensity and stability of distinct materials. Many reports studied colloidal semiconductors such as quantum dots, which the main properties are strongly based in their particle size [10–15], rare earth nanoparticles (NPs), systems which increase the emission quantum yield due to  $f$  transitions in the shell environment [16–18], and noble metal NPs due to their inert nature [19–21]. Recently, carbon NPs and carbon dots have emerged for this application [22–26].

Specifically, luminescent NPs comprising the calcium orthophosphate (CaP) family are interesting for forensic purposes. This is mainly due to their superior biodegradability, biocompatibility and easily scalable synthetic routes [27,28]. However, current research based on luminescent CaPs NPs, mainly focused on hydroxyapatite (HA) and amorphous calcium phosphates (ACPs), pointed towards other technological fields such as nanomedicine [29]. These NPs have received much attention mainly due to the high capacity to incorporate foreign ions, such as lanthanide ions, that allow the improvement of their luminescence properties [30].

On the other hand, Zollfrank *et al.* [31] and Aronov *et al.* [32,33] demonstrated the occurrence of intrinsic photoluminescence (PL) in HA and attributed this behavior to the presence of defect-related localized energy states. Since then, self-activated luminescence mechanisms in HA micro- and nanoparticles have been studied by several research groups [34–42], and were optimized for monitored drug delivery [44–48], bioimaging [49–51], biosensing [51,52], and secure information storage [53]. The main advantages of these strategies are that HA is made up of earth-abundant and relatively low-cost elements, where

the achievement of intense luminescence avoids the need of doping with activator species. Also, the intrinsic luminescence was employed as a method to characterize HA-based photocatalysts [54], structural and compositional changes in bones [55,56], and in early caries detection [57].

In this study, the correlation between structural, optical, PL properties of ACP NPs were characterized for the first time and compared with those of HA NPs. ACP has significant structural resemblances with HA and is the first CaP phase precipitated from supersaturated aqueous solutions at the initial stages of the reaction between calcium and phosphate ions [58]. Hence, ACP can be prepared by faster and easier synthetic routes such as chemical precipitation. However, special attention is necessary to avoid its spontaneous crystallization in other CaPs. In the present work, ACP NPs were washed and recovered 1 min after precipitation. The post heat treatment step conducted at 400 °C plays a two-fold role. First, to increase ACP phase stability, a well know strategy to obtain stable powders at room temperature [59], and second, to improve the luminescent properties of ACP NPs, a crucial step observed for other CaPs [36,49]. Based on these results, this study allows the establishment of non-toxic and stable luminescent ACP NPs to be used for sensitive development of latent fingerprints.

### **4.3. Materials and methods**

#### **4.3.1. Materials**

Calcium nitrate tetrahydrate ( $\text{Ca}(\text{NO}_3)_2 \cdot 4\text{H}_2\text{O}$ , 99%) was purchased from Sigma-Aldrich and di-ammonium phosphate ( $(\text{NH}_4)_2\text{HPO}_4$ , 98+%) from Strem Chemicals. Ammonium hydroxide, absolute ethanol, and acetone were purchased from Labsynth. Human Dermal Fibroblast neonatal (HDFn, catalog number C0045C) cell line was purchased from Thermo Fischer Scientific. Dulbecco's Modified Eagle's Medium (DMEM) and Fetal Bovine Serum (FBS) were purchased from Vitrocell. MTT (3-[4,5-dimethylthiazol-2-yl]-2,5-diphenyltetrazolium bromide) was purchased from Sigma-Aldrich, and dimethyl sulfoxide (DMSO) from Labsynth. All reagents were used as received without further purification.

### 4.3.2. Synthesis

The amorphous calcium phosphate ACP NPs were synthesized via an easy approach based on chemical precipitation. First, 50 mL of an aqueous phosphate solution (6 mmol of  $(\text{NH}_4)_2\text{HPO}_4$ , pH ~ 8.5) and 100 mL of an aqueous calcium solution (10 mmol,  $\text{Ca}(\text{NO}_3)_2 \cdot 4\text{H}_2\text{O}$ , pH ~ 6.8) were placed in separated flasks under vigorous stirring at room temperature. The pH values of both solutions were adjusted to ~10 by adding ammonium hydroxide. Then, the phosphate solution was added to calcium solution by one-batch step and the resulting mixture was stirred for 1 min. The solid product was recovered and washed thoroughly by centrifugation with water and acetone. The resulting slurry was dried at 60 °C for 4 h in air and is referred to as ACP sample. Then, the ACP powder was placed in alumina crucible and heat treated at 400 °C/4h in a programmable furnace at a heating rate of 10 °C/min. The sample was then naturally cooled to room temperature and is referred to as the ACP400 sample. Comparatively, we also allowed the crystallization of ACP in HA structure by increasing the aging step from 1 min to 24h for a fraction of the resulting calcium and phosphate mixed solution described above. In this case, the solid product was recovered and washed several times with water and ethanol by centrifugation and dried over night at 80 °C. The HA sample was heat treated at 400 °C/4h in the same conditions than those used for ACP powder and is referred to as the HA400 sample.

### 4.3.3. Characterization

Transmission electron microscopy (TEM) was performed in a FEI TECNAI F20 (Netherlands) microscope operating at 200 kV. The prepared samples were structurally characterized by X-ray diffraction (XRD) in a Shimadzu XRD-6000 (Japan) diffractometer using  $\text{Cu K}\alpha$  radiation ( $\lambda = 0.154184$  nm). The data were collected using a step scan rate and step size of 0.2°/min and 0.02°, respectively. Fourier transform infrared (FTIR) spectroscopy was performed using a Nicolet iS50 spectrometer (Thermo Scientific, USA) operated in absorbance mode. The spectra were recorded at a resolution of 4  $\text{cm}^{-1}$  over the wavenumber range of 400 - 4000  $\text{cm}^{-1}$ . The peak asymmetry ( $\Delta S$ ) was estimated according to Equation 1 [60,61]:

$$\Delta S = (H_R - H_L)/(H_R + H_L) \quad (1)$$

Where  $H_R$  and  $H_L$  are the right and left components of the full width at half

maximum (FWHM) of the  $\nu_3\text{PO}_4$  and  $\nu_4\text{PO}_4$  bands.

X-ray photoelectron spectroscopy (XPS) studies were performed on a Physical Electronics PHI VersaProbe II spectrometer using monochromatic Al- $K_\alpha$  radiation (49.1 W, 15 kV and 1486.6 eV) for analyzing the core-level signals of the elements of interest with a hemispherical multichannel detector. The sample spectra were recorded with a constant pass energy value at 29.35 eV, using a 200  $\mu\text{m}$  diameter circular analysis area. The XPS spectra obtained were analyzed using PHI SmartSoft software and processed using a MultiPak 9.3 package. The binding energy values were referenced to adventitious carbon C 1s signal (284.8 eV). Shirley-type background and Gauss-Lorentz curves were used to determine the binding energies. Ultraviolet-visible (UV-Vis) spectroscopy was performed using a Shimadzu UV-2600 (Japan) spectrophotometer operated in diffuse-reflection mode. Excitation and emission PL spectra were acquired in a Horiba Jobin Yvon spectrofluorometer model Fluorolog-3, equipped with a 450 W Xe lamp as the excitation source. Signals were collected by a visible photodiode detector model PPD-850. All spectra were corrected by the lamp profile and detector response. PL spectroscopy was also conducted at room temperature by a Kimmon IK5451R-E HeCd laser ( $\lambda_{\text{exc}} = 450 \text{ nm}$ ) and using a Coherent Innova 200 K krypton laser (USA) ( $\lambda_{\text{exc}} = 405 \text{ nm}$ ) was used as the excitation sources.

#### 4.3.4. Cytotoxicity assay

HDFn cells were used to investigate the potential cytotoxicity of ACP400 NPs in order to probe if the NPs are safe to be used for forensics purposes. Cells were cultured as a monolayer in DMEM supplemented with 10% v/v inactivated FBS, at 37 °C and 5% CO<sub>2</sub>. For cell viability analysis, they were seeded onto a 96-well microplate at  $2 \times 10^4$  cell/mL. After 24 h, the medium was replaced with fresh complete medium containing the NPs at different concentrations (0, 20, 40, 80, 160 and 320  $\mu\text{g/mL}$ ) and cells were incubated for 24 and 48 h. At the end of the exposure periods, HDFn cells were incubated with 0.5 mg/mL of MTT for 2 h, washed with phosphate-buffered saline and formazan was solubilized with 200  $\mu\text{L}$  of DMSO. The absorbance was recorded at 570 nm using a SpectraMax M3 (Molecular Devices) plate reader. Three independent experiments with three replicates each were conducted. Data distribution was tested, and one-way analysis of variance (ANOVA) tests were performed, followed by Dunnett's post-test. Cytotoxicity was investigated by the comparison of the controls versus groups containing the NPs. *p*-values less than 0.05 were considered to be statistically significant.

#### 4.3.5. Fingerprint imaging

Fingerprints recorded were analyzed to be validated by IAFIS system (3M Cogent's Integrated Automated Fingerprint and Palm Print Identification System), a customizable software package that allows to perform a wide range of tasks for processing, editing, searching, retrieving, and storing fingerprint images and subject records used by Scientific Police in Spain. The acquisitions of the fluorescent fingerprints on the different surfaces were conducted by a Polilight PL10 (Rofin Australia). Excitation bands in NUV region ( $\lambda_{exc} = 350$  and  $450$  nm) were used with yellow goggles (495 nm, edge wavelength) and orange goggles (edge wavelength 550 nm), respectively. The 450 nm excitation conditions produced superior images to NUV and further work was confined to this wavelength. The images of latent fingerprints were obtained using a Multi-zoom Nikon AZ-100 microscope and a NikonDigital Sight-5Mc, connected to the microscope by a computer, in which the pictures were stored and visualized by NIS-Elements software. The microscope was equipped with an epifluorescence system, in which the samples were illuminated by a mercury lamp (100 W) and a variety of available filter blocks (UV-2A: EX 330-380; DM 400; BA 420) were used.

### **4.4. Results and discussion**

#### 4.4.1. Morphology and long-range ordering (LRO) analysis

The morphological aspects of the as-prepared ACP and ACP400 samples were investigated by TEM, and the obtained images are displayed in **Figures 1a-b**, respectively. Both samples are composed of chain-like NPs with irregular rounded shape and diameters ranging mainly from 10 to 40 nm. No significant difference of the morphological aspects was observed between ACP and ACP400 samples. The selected area electron diffraction (SAED) pattern of the ACP400 NPs shows a typical pattern of an amorphous material (inset **Figure 1b**). The chemical composition of ACP400 sample was evaluated by energy-dispersive X-ray Spectroscopy (EDS) (**Figure 1c**), indicating the presence of Ca, P, and O elements, which consist of the main constituents of ACP structure. The presence of C can be mainly attributed to the carbon film of TEM grid.



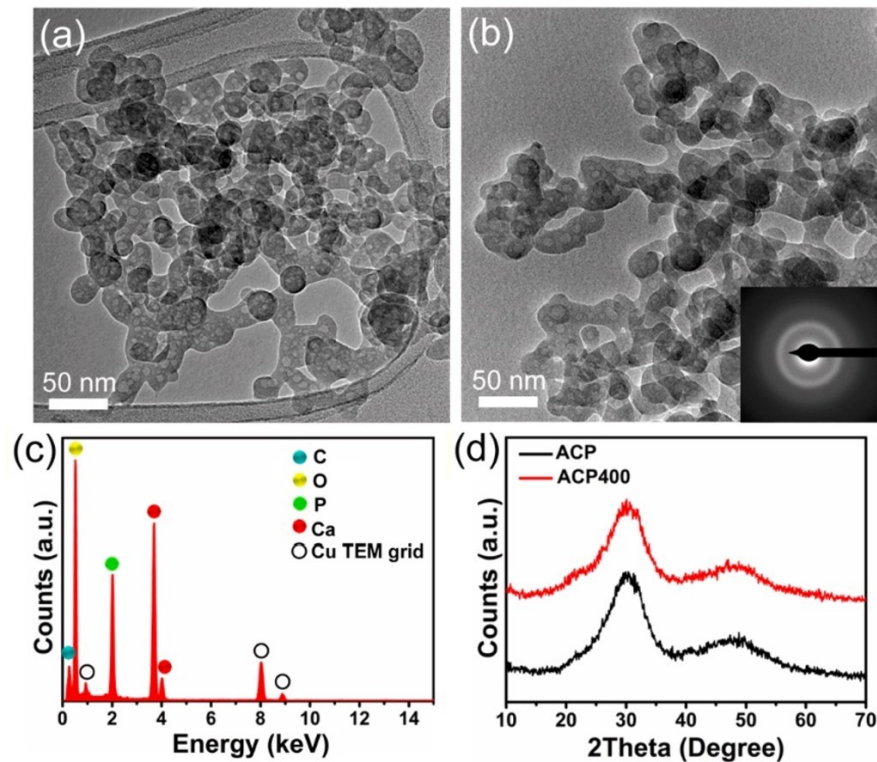


**Figure 1.** TEM micrographs corresponding to (a) ACP and (b) ACP400 NPs (SAED pattern, inset), (c) EDS elemental analysis of ACP400 NPs, and (d) XRD patterns of prepared samples.

The chemical composition of ACP400 sample was evaluated by energy-dispersive X-ray Spectroscopy (EDS) (**Figure 1c**), indicating the presence of Ca, P, and O elements, which consist of the main constituents of ACP structure. The presence of C can be mainly attributed to the carbon film of TEM grid. Ca/P molar ratio calculated by EDS analysis resulted in 1.43, which is close to but slightly lower than the value obtained for amorphous tricalcium phosphate (ATCP, Ca/P = 1.50), with general formula  $\text{Ca}_3(\text{PO}_4)_2$ . This was also found in a recent report for ACP samples synthesized in similar conditions [62]. Such decrease in Ca/P ratio is mostly related to the presence of acidic phosphate groups ( $\text{HPO}_4^{2-}$ ) substituting  $\text{PO}_4^{3-}$  groups in the initial ACP NPs (see section 3.2), which is a well-known substitution in almost all ACP samples synthesized at  $\text{pH} < 11$  [63]. These groups lowers the Ca/P ratio by generating calcium vacancies ( $V_{\text{Ca}}$ ) in order to keep the electroneutrality in ACP structure [64].

**Figure 1d** shows the XRD patterns of the ACP sample precipitated at room temperature. No discernible peaks of crystalline CaP phases were observed. Instead, the broad diffraction halo at  $2\theta = 30^\circ$  indicates that an amorphous phase which lack of LRO was preserved [65]. A poorly crystallized phase only appears when increasing the reaction time to

24h (**Figure S1a**), which is related to the spontaneous conversion of ACP to calcium-deficient HA ( $\text{Ca}_{10-x}(\text{HPO}_4)_x(\text{PO}_4)_{6-x}(\text{OH})_{2-x}$  ( $0 < x < 1$ )) in the mother solution [58]. As also shown in **Figure 1d**, the amorphous pattern of ACP sample persists after conducting the heat treatment at 400 °C for 4h (ACP400 sample). The thermally induced crystallization of ACP sample was only observed when annealing it at higher temperatures (600 °C/4h), where peaks corresponding to the monoclinic  $\alpha$ -tricalcium phosphate ( $\alpha$ -TCP,  $\alpha$ - $\text{Ca}_3(\text{PO}_4)_2$ ) phase were discernible (**Figure S2**). ACP is known to assume a hydrated TCP-resemble structure with the experimental conditions adopted [61,66], and posterior annealing procedures ( $T \geq 600$  °C) mainly lead to a solid state reordering of ACP in the crystalline TCP phases [67].

Considering that thermal stability is a critical parameter for long term use of ACP in practical applications, a further thermal aging treatment of ACP400 NPs was conducted at 80 °C/8h, based on a recent report [68]. No evidence of crystalline phases was observed after conducting this experiment (**Figure S3**), which assures the thermal stability of our ACP400 sample.

#### 4.4.2. Short-range ordering (SRO) analysis

**Figure 2a** shows the FTIR spectra obtained for ACP and ACP400 samples. The main vibrational modes of  $\text{PO}_4^{3-}$  groups are observed, including the asymmetric stretching mode of P–O bond ( $\nu_3$ ) in the 1300 - 900  $\text{cm}^{-1}$  range, as well as the symmetric stretching mode of P–O bond ( $\nu_1$ ) appearing as a shoulder, and the bending mode of O–P–O bond ( $\nu_4$ ) in the 685 - 485  $\text{cm}^{-1}$  range [69]. The broad and unsplitted  $\nu_3$  and  $\nu_4$  modes herein observed are characteristic of ACP phase [70,71]. The presence of these vibrational bands evidences a certain degree of SRO of atomic groups in ACP and ACP400 NPs despite the lack of structural LRO detected by XRD.

A band with very weak intensity can be seen near 2300  $\text{cm}^{-1}$  (**Figure S4a**) and is attributed to H–O(P) stretching mode of  $\text{HPO}_4^{2-}$  groups [72], confirming their presence in our ACP sample. The doublet between 1600–1375  $\text{cm}^{-1}$  are assigned to the asymmetric stretching mode of C–O bond ( $\nu_3$ ) of  $\text{CO}_3^{2-}$  group, whereas the low intensity band centered at 871  $\text{cm}^{-1}$  is related to the bending mode of O–C–O bond ( $\nu_2$ ) of this same group [69]. The presence of  $\text{CO}_3^{2-}$  impurity is typically associated to the precipitation of ACP under atmospheric conditions, which causes the solubilization of  $\text{CO}_2$  from air followed by the slight incorporation of the resulting  $\text{CO}_3^{2-}$  groups in the amorphous material by the substitution of

$\text{PO}_3^-$  groups [73]. This substitution renders a global slightly increase in Ca/P molar ratio values, despite additional  $V_{\text{Ca}}$  vacancies are formed for charge balance implications. Based on the pertinent literature [62,63], we conclude that the Ca/P molar ratio of 1.43 found in ACP400 sample is a net result of the simultaneous presence of  $\text{HPO}_4^{2-}$  and  $\text{CO}_3^{2-}$  groups in precipitated ACP sample. Lastly, the bands associated to the vibrational modes of water molecules are observed in the range  $3700 - 2500 \text{ cm}^{-1}$  and at  $1655 \text{ cm}^{-1}$  [74].

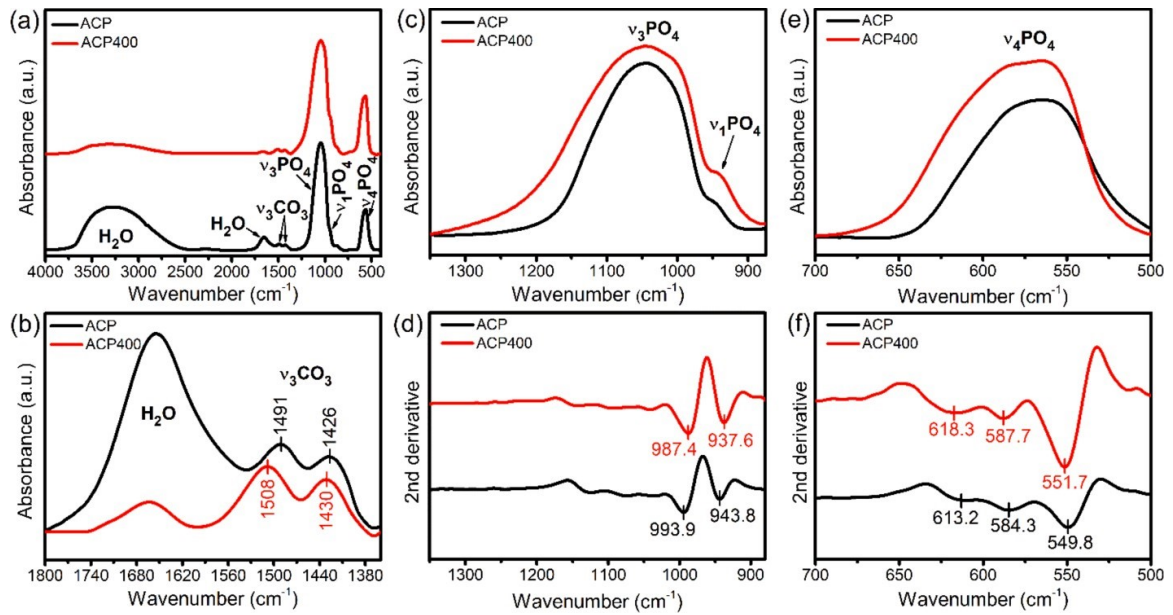


**Figure 2.** (a) FTIR spectra of ACP and ACP400 samples, (b) magnified view of  $\text{H}_2\text{O}$  and  $\text{v}_3\text{CO}_3$  bands, (c,e) magnified views of  $\text{v}_3/\text{v}_1\text{PO}_4$  and  $\text{v}_4\text{PO}_4$  bands, respectively, and (d,f) 2<sup>nd</sup> derivative spectra of  $\text{v}_3/\text{v}_1\text{PO}_4$  and  $\text{v}_4\text{PO}_4$  bands, respectively.

As shown in **Figures 2a-b**, a remarkable difference between FTIR spectra of ACP and ACP400 is the intensity of  $\text{H}_2\text{O}$  bands, which significantly decreases in the latter sample. Eanes [67] demonstrated that chemically precipitated ACP obtained at similar alkaline conditions ( $\text{pH} = 9.5-10$ ) can retain  $\sim 15 \text{ wt}\%$  of water even after lyophilization. Holmes and Beebe [75] concluded that  $\sim 25\%$  of this value corresponds to adsorbed water, whereas  $\sim 75\%$  are tightly bounded water molecules inside ACP structure. More recently, Uskoković *et al.* [61] corroborated with these seminal studies by obtaining similar water contents of  $16.8 \text{ wt}\%$  in which  $30\%$  are adsorbed on ACP surface and  $70\%$  are inside the solid framework. Therefore, the dehydration observed in ACP400 sample of the present work are mainly associated to the irreversible elimination of these water molecules inside the ACP structure that occurs in the  $25 - 400 \text{ }^\circ\text{C}$  temperature range and, in a less extend, to the

reversible loss of adsorbed water [59,61,75].

As mentioned earlier, the presence of  $\text{HPO}_4^{2-}$  groups in ACP sample (**Figure S4a**) is typically detected in amorphous ACP phases [76,77], and is in agreement with the general formula of ACP,  $\text{Ca}_x\text{H}_y(\text{PO}_4)_z \cdot n\text{H}_2\text{O}$  ( $n = 3-4.5$ ) [58]. However, it disappears upon heating (ACP400 sample) accompanied by the appearance of another weak band at  $\sim 730 \text{ cm}^{-1}$  (**Figure S4b**). This new band is associated to  $\text{P}_2\text{O}_7^{4-}$  formed by the condensation of  $\text{HPO}_4^{2-}$  groups according to the thermally-induced reaction  $2\text{HPO}_4^{2-} \rightarrow \text{P}_2\text{O}_7^{4-} + \text{H}_2\text{O}\uparrow$  [72,78]. According to Eanes [67], even though there is an elimination of water from ACP lattice by this reaction, the water lost by heating is predominantly related to dehydration due to the low concentration of  $\text{HPO}_4^{2-}$  groups in the initial amorphous material.

As shown in **Figures 2c,e**; a broadening in the  $\text{PO}_4^{3-}$  bands related to internal, short-range  $\nu_3$  and  $\nu_4$  vibrational modes when ACP NPs are heat treated at  $400 \text{ }^\circ\text{C}$  is observed, reflecting in an increase of FWHM values from, respectively, 150 and  $77 \text{ cm}^{-1}$  for ACP NPs to 190 and  $90 \text{ cm}^{-1}$  for ACP400 NPs. These values represent a FWHM increase of 27% ( $\nu_3$ ) and 17% ( $\nu_4$ ) in ACP400. Moreover, the  $\nu_3$  and  $\nu_4\text{PO}_4^{3-}$  bands have become more asymmetrical in shape by the heating procedure, leading to a peak asymmetry ( $\Delta S$ ) of, respectively, 0.14 and 0.16 for ACP NPs to 0.21 and 0.23 for ACP400 NPs, which means a  $\Delta S$  increase of 50% and 44%, respectively, for these bands. As stated by Uskoković [60], these data can be interpreted as a decrease in SRO into  $\text{PO}_4^{3-}$  groups of ACP400 NPs with a consequent larger absorption of varied frequencies although temperature-related structural changes usually tend to lead higher degrees of structural ordering in materials. As previously discussed, an important loss of tightly bounded water occurred in ACP400 (**Figures 2a-b**). This liberation is known to lead to an overall contraction in ACP lattice to remove empty spaces [60]. Hence, the structural shrinkage significantly increases the lattice strain and led to even more distorted environments around the  $\text{PO}_4^{3-}$  clusters, reflecting in the asymmetrical broadening of  $\nu_3$  and  $\nu_4\text{PO}_4^{3-}$  modes due to fluctuations in P–O bonds length and in the O–P–O bond angles inside the  $\text{PO}_4^{3-}$  structure.

A further evidence of structural changes in the  $\text{PO}_4^{3-}$  groups and their neighborhoods by annealing at  $400 \text{ }^\circ\text{C}$  is the redshift of one observable component for the triply degenerated asymmetric stretching mode ( $\nu_3$ ) from  $994$  to  $988 \text{ cm}^{-1}$ , the redshift of the non-degenerated symmetric stretching mode ( $\nu_1$ ) from  $943$  to  $937 \text{ cm}^{-1}$  and, in opposite, the

blueshift of all components of the triply degenerated bending mode ( $\nu_4$ ) from 612, 585, 550 to 618, 588, 553  $\text{cm}^{-1}$ , respectively, as analyzed by the second-derivative plots (**Figures 2d,f**). This effect is associated to stronger interactions of  $\text{PO}_4^{3-}$  groups with the near-neighbor atoms into the ACP shrunken lattice that occurs at temperatures below the amorphous-to-crystalline phase transition [60].

In  $\nu_3$  bands of  $\text{CO}_3^{2-}$  groups (**Figure 2b**) important features are sensed after the heat treatment procedure: (i) a slight decrease in intensity of the doublet, which is associated to a partial sublimation of this impurity as  $\text{CO}_2$  at 400 °C [60], (ii) a blueshift of the doublet from 1491 and 1426  $\text{cm}^{-1}$  to 1508 and 1430  $\text{cm}^{-1}$ , and (iii) a slight increased separation of the doublet from 65 to 78  $\text{cm}^{-1}$ . These last two characteristics of  $\nu_3$  modes are sensitive to the structural location of  $\text{CO}_3^{2-}$  impurities in CaPs [78] and are susceptible to changes in the amount of hydration water into lattices with surrounds that strongly interact with these groups [79–82]. In this sense, the present results indicate that the remaining  $\text{CO}_3^{2-}$  groups were influenced by the compositional and organizational changes at the surroundings due to the water loss and lattice contraction, leading to different *stereo*-chemistries for  $\text{CO}_3^{2-}$  groups with more energetic C–O bonds.

#### 4.4.3. Surface analysis

The surface chemical composition of ACP400 sample is based on O 1s (53.9 at.%), C 1s (17.2 at.%), P 2p (12.8 at.%), and Ca 2p (16.1 at.%), as detected on the survey scan (**Figure 3a**). Basically, the XPS analysis showed that the most key information was found in the C 1s signal (**Figure 3b**), which can be deconvoluted in three main contributions. A main peak at 284.8 eV is mostly attributed to surface hydrocarbon chains after heat treatment at 400 °C (C–C/C–H bonds); the further two shoulders at 286.8 and 289.1 eV are assigned to C–O and C=O (carbonyl)/O=C–O<sup>-</sup> (carboxyl bonds), respectively, which are attributed to  $\text{CO}_3^{2-}$  on the surface of ACP400 NPs [83]. Moreover, O 1s was deconvoluted in three main contributions at 531.0 (C=O), 533.1 (C–O/P=O) and 534.7 eV (P–O) [84] (**Figure 3c**). These results indicate the presence of graphitized carbon and  $\text{CO}_3^{2-}$  groups from ACP. The other peaks related to P 2p do not show relevant inputs. The signal attributed to the  $\text{PO}_4^{3-}$  component showed a single peak, indicating that all the P atoms have an equivalent environment.

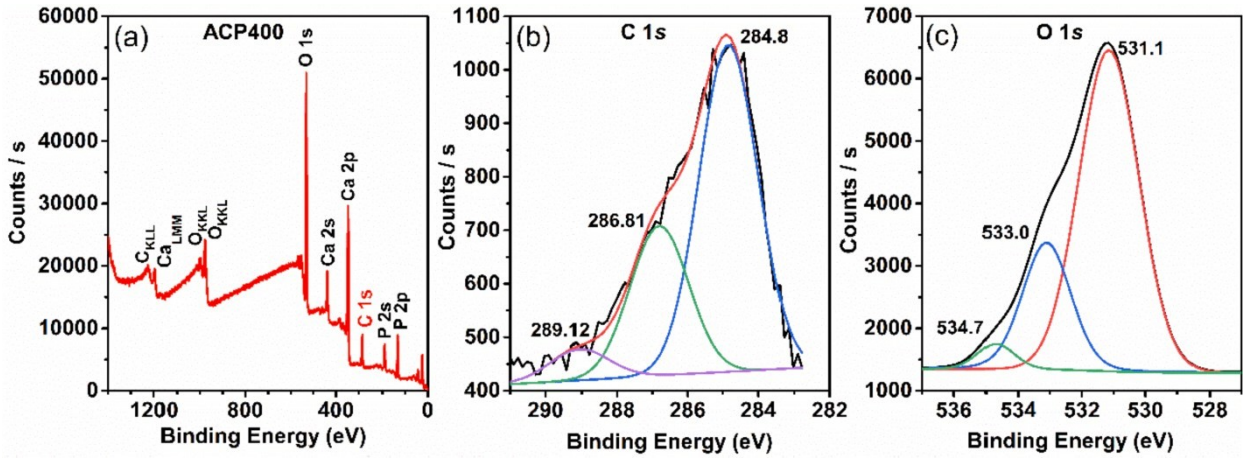


**Figure 3.** (a) Survey XPS spectrum of ACP400 NPs. High-resolution XPS spectra of (b) C 1s and (c) O 1s.

#### 4.4.4. Optical properties

In a semiconductor, the optical band gap energy ( $E_g$ ) describes the energy needed to excite an electron from the valence band (VB) to the conduction band (CB).  $E_g$  can be estimated by the Tauc's method according to Equation 2:

$$(\alpha h\nu)^{1/n} = A(h\nu - E_g) \quad (2)$$

Where  $\alpha$  is the absorption coefficient,  $h\nu$  is the incident photon energy,  $A$  is a constant depending on the transition probability, while  $n$  is equal to 1/2 or 2 for direct and indirect transition bandgaps, respectively [79]. The diffuse reflectance spectroscopy is often used to determine the  $E_g$  value, and **Figure S5** illustrates the reflectance spectra obtained for ACP and ACP400 samples. The Kubelka-Munk function,  $F(R_\infty)$ , can be derived from these spectra as given by Equation 3:

$$F(R_\infty) = \frac{(1-R_\infty)^2}{2R_\infty} = \frac{\alpha}{s} \quad (3)$$

Where  $R_\infty$  is the reflectance and  $s$  is the scattering coefficient.  $F(R_\infty)$  is proportional to  $\alpha$  if  $s$  is assumed to be wavelength independent and can substitute  $\alpha$  in Equation 3 [80]. The plot of  $[F(R_\infty)h\nu]^{1/n}$  vs.  $h\nu$  leads to the Tauc's plot, and the  $E_g$  value is obtained by fitting and extrapolating the linear portion of the plot to the energy axis. **Figures 4a-b** show the Tauc's plots of our samples considering the previous approach. Additionally, we also used a linear fit as the abscissa (blue dotted line) for each spectrum

presenting significant sub-bandgap absorption. According to Makuła *et al.* [81], the use of this baseline method leads to more accurate estimation of  $E_g$  value by the intersection of the two fitted lines.

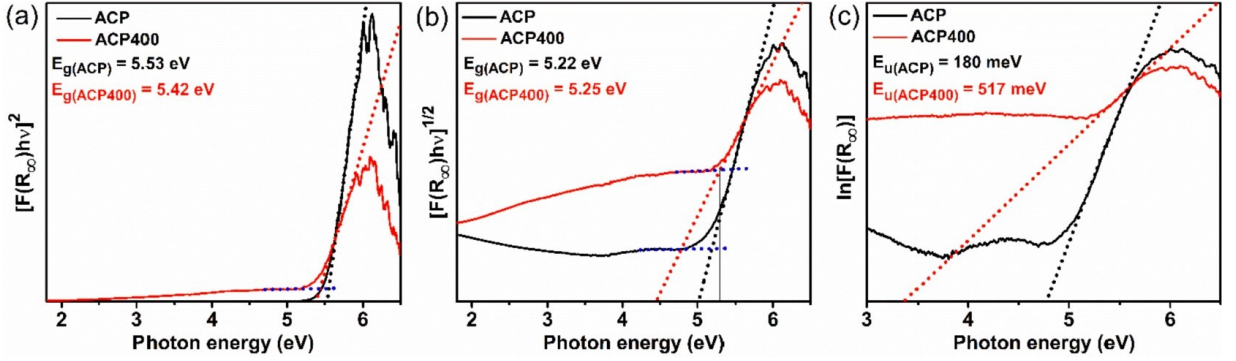


**Figure 4.**  $E_g$  and  $E_u$  energies for ACP and ACP400 samples. Tauc's plots for (a) direct transition ( $n = 1/2$ ) and (b) indirect transition ( $n = 2$ ). (c) Plots of  $\ln[F(R_\infty)]$  vs. photon energy.

Herein, two important insights can be highlighted. First, the  $E_g$  values calculated for both ACP ( $E_g = 5.53$  and  $5.42 \text{ eV}$  for  $n = 1/2$  and  $2$ , respectively) and ACP400 samples ( $E_g = 5.22$  and  $5.25 \text{ eV}$  for  $n = 1/2$  and  $2$ , respectively) are closely related to those found in crystalline CaPs, including  $\alpha$ -TCP ( $E_g = 4.89 \text{ eV}$ ) and  $\beta$ -TCP ( $E_g = 5.25 \text{ eV}$ ) [88], with direct bandgap transitions, as well as HA ( $E_g = 4.51\text{--}5.78 \text{ eV}$ ) [36,89–93] and Ca-dHA ( $E_g = 5.67 \text{ eV}$ ) [94], with indirect bandgap transitions. The band structures of these materials are mainly composed by overlapped P  $3s$ , P  $3p$  and O  $2p$  orbitals from covalent  $\text{PO}_4^{3-}$  groups at the upper VB, with minor contributions of Ca  $4s$  and  $3d$  components due to ionic interactions of Ca with O from neighboring  $\text{PO}_4^{3-}$  groups, as well as components from OH groups in the case of HA and Ca-dHA, whereas the bottom of CB is mainly composed by Ca  $3d$  components [88–91,94]. Since SRO is the key feature for the electronic properties of a solid [85], we can assume that the close  $E_g$  values between our ACP samples and those found for other CaPs emerge from the structural similarities at short-range between the amorphous and crystalline phases, leading to comparable band structures.

Second, a decrease in  $E_g$  from  $5.53$  to  $5.42 \text{ eV}$  (**Figure 4a**) is observed by conducting the heat treatment at  $400 \text{ }^\circ\text{C}/4\text{h}$ . This decrease is accompanied by an increment in tailing of band states extending within the forbidden gap. In poorly crystalline and amorphous materials, the presence of these tails of energy states instead of sharp band-edge absorptions is characteristic of a broad distribution of defect levels which vary upon the degree of lattice disorderliness [95]. The tail absorption exponentially depends on photon energy, and the plot

of  $\ln[F(R_\infty)]$  vs.  $h\nu$  can be used to calculate the Urbach energy ( $E_u$ ) or Urbach tail width by the slope of the straight line obtained in this plot. In our case,  $E_u = 180$  and  $517$  meV for ACP and ACP400, respectively, as shown in **Figure 4c**. The  $E_g$  decrease and  $E_u$  increase after the heat treatment step could be attributed to an increment in lattice disorder (lower degree of SRO) for ACP400 compared to ACP sample, due to the wider deviations of bond lengths and bond angles from the ideal values, as was also observed by FTIR data (section 3.2).

#### 4.4.5. PL properties

**Figures 5a-b** show the excitation spectra of ACP and ACP400 NPs recorded by monitoring the main PL emission at  $\lambda_{em} = 530$  and  $540$  nm, respectively. A broad and intense band centered at  $243$  nm ( $5.10$  eV) is sensed in both samples and can be attributed to the excitation departing from band states and localized tail states. The inset of each figure shows a magnified view over a selected wavelength region ( $260 - 520$  nm). A weak but clear band extending up to  $500$  nm with maxima at  $370$  nm ( $3.35$  eV) and  $398$  nm ( $3.12$  eV) is observed in ACP NPs. On the other hand, this region in ACP400 NPs is composed by a weak band in the  $300 - 375$  nm range with maximum at  $317$  nm ( $3.91$  eV), as well as by a band in the  $400 - 520$  nm range with maxima at  $456$  nm ( $2.72$  eV) and  $484$  nm ( $2.56$  eV). As the excitation energies are much lower than  $E_g$  values in both samples, these bands can be attributed to excitation involving localized energy states from point defects in ACP structure, as were also observed in other materials with similar spectral features [96]. These data evidence that there is an important reorganization of the energy levels within the band gap in ACP by conducting the thermal treatment.

**Figure 5c** shows the PL emission spectra of ACP and ACP400 NPs recorded at  $\lambda_{exc} = 450$  nm. The excitation wavelength was selected to resemble the one employed in fingerprint analysis. Both samples exhibited broadband emission profiles originated from radiative recombination of electron-hole pairs ( $e^-h^+$ ) through pathways which can encompass extended energy states as well as countless localized energy states. Considering that both the excitation and emission wavelengths have significantly lower energies than the  $E_g$  calculated, the contribution of band-to-band transitions between extended energy states is negligible. The emission band of ACP NPs ranges from  $490$  to  $740$  nm and reaches its maximum of intensity at  $530$  nm ( $2.34$  eV), whereas for ACP400 NPs the emission band is broader and falls into the  $490 - 800$  nm range with maximum at  $540$  nm ( $2.30$  eV). Another remarkable feature observed in PL spectra is the expressive increase in intensity by at least  $50$  times after the heat



treatment of the NPs at 400 °C.

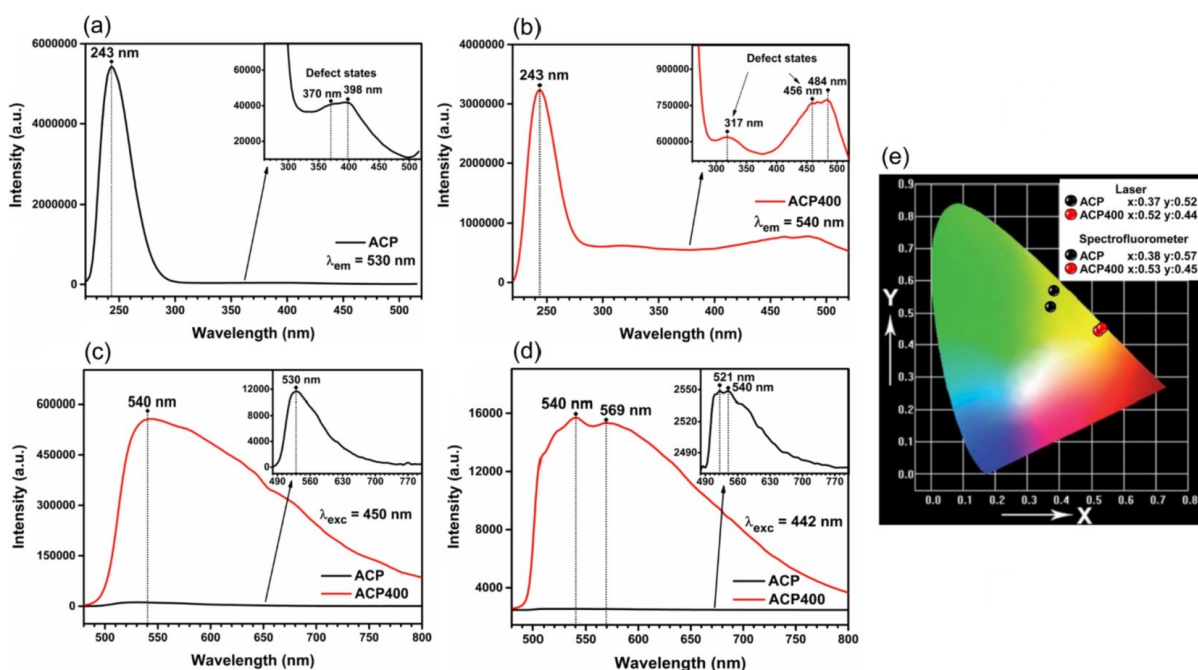


**Figure 5.** (a,b) PL excitation spectra of ACP and ACP NPs, respectively. PL emission spectra obtained by a (c) spectrofluorometer ( $\lambda_{exc} = 450$  nm) and (d) HeCd laser ( $\lambda_{exc} = 442$  nm). (e) Calculated CIE chromaticity coordinates from the PL emission spectra.

To evaluate the effect of distinct excitation sources on the PL properties of the prepared samples, the emission spectra were also recorded using the 442 nm line of HeCd laser (**Figure 5d**). Only a minor change on the inclination of the bands at shorter wavelengths is sensed due to the distinct configuration of the optical filters employed, as well as a slight increase in the resolution of the emission bands when compared to the spectra acquired via spectrofluorometer, i.e., the maxima of the bands are now centered at 521 and 540 nm for ACP NPs and at 540 and 569 nm for ACP400 NPs. This feature is mainly related to the narrower excitation line of the laser source.

The distinct characteristics observed between the emission profiles of ACP and ACP400 NPs (**Figures 5c-d**) influenced the color of PL observed, mainly associated to the increase on the relative contribution of radiative emissions at longer wavelengths in ACP400 sample. **Figure 5e** shows the *Commission Internationale de l'Éclairage* (CIE) chromaticity diagram. The CIE coordinates shifted from  $x = 0.38/0.37$  and  $y = 0.57/0.52$  for ACP to  $x = 0.53/0.52$  and  $y = 0.45/0.44$  for ACP400 (spectrofluorometer/laser), corresponding to green-yellow and yellow-orange regions, respectively. Also, the close-related CIE coordinates for both excitation sources confirm the reproducibility of the emission profiles using distinct

luminescence techniques and indicate that the color of the PL observed was not considerably affected. The broadening and red shift of the emission band with a consequent change in emission color observed in **Figure 5e** is often associated to a decrease in structural ordering in materials [97–99], confirming that ACP400 exhibits a higher degree of lattice disorder than the ACP sample induced by the heat treatment procedure employed in this study.

#### 4.4.6. Hypotheses for PL properties of ACP

The nature of the PL properties in ACP are not completely clear yet, but according to this study the determining factor is the presence of localized energy states due to order-disorder effects. In the last years, the electronic structure and PL properties of HA were studied due to its potential applications in optical devices and in nanomedicine [29], but no previous literature was found concerning the ACP structure. In this sense, to better elucidate the nature of PL emissions in the amorphous NPs, we measured the emission spectra of ACP after allowing its conversion into calcium-deficient HA, and the results are illustrated in **Figures 6a-c**. In this case, we excited our samples at  $\lambda_{\text{exc}} = 405$  nm with a higher energy laser source to allow the comparison of the results with those of former published studies [36,39]. Interestingly, both amorphous (ACP) and poorly crystallized (HA) samples presented broadbands with comparable profiles. A plausible reason for the similar PL emission spectra after ACP→HA transition could be explained based on their structures at short-range.

ACP NPs were proposed to exhibit SRO due to the presence of randomly packed  $\text{Ca}_9(\text{PO}_4)_6$  units with an average size of 9.5 Å (Posner's clusters) [65] which, in turn, resemble a spatial subset of  $\text{Ca}^{2+}$  and  $\text{PO}_4^{3-}$  in HA unit cell [58]. The mechanisms governing the ACP→HA transition are not yet fully understood, but it is well-accepted that there is key role of aqueous environments for the occurrence of solid-state reorganization, dissolution/reprecipitation, self-assembly aggregation and partial dissolution-aggregation mechanisms [77,100]. More to the point, several studies experimentally confirmed the existence of the proposed Posner's clusters and that these basic pre-nucleation clusters are conserved during ACP→HA transformation [77,101,102]. As to say, although there is a LRO increase in the ACP→HA phase transition with the presence of translational symmetry and stricter distribution of environments in HA structure, both materials possesses similarities at short and medium range spatial organization of atomic groups [58,60], which could result in comparable atomic interactions and electronic structures (see section 3.4), as was also

observed in other amorphous/crystalline semiconductors [85].

Considering the previous discussion, it is also plausible that the order-disorder effects which govern the PL for chemically precipitated ACP and HA samples have similar nature. In HA, the PL emission was proposed to arise mainly from perturbations of Ca and PO<sub>4</sub> electronic densities which led to new acceptor and donor-like localized states inside the band gap [37]. These states arise from the VB and CB, respectively, with Ca 3*p*, Ca 4*s*, P 3*s*, P 3*p*, O 2*s*, and O 2*p* character [103]. This lattice disorder was mainly attributed to ionic vacancies ( $V_{Ca}$ ,  $V_H$ ,  $V_{OH}$ , and  $V_O$  in PO<sub>4</sub><sup>3-</sup> groups) and to distortions in the bond's lengths and angles of the structural coordination clusters [35,37,40,103,104]. Some reports also concluded that CO<sub>3</sub><sup>2-</sup> impurity and the defects associated to its stabilization in HA lattice could contribute to the defect-related PL emission [39,45,49].

In ACP NPs, perturbations in Ca and PO<sub>4</sub> electronic densities could occur due to fluctuations in Ca–O and P–O bonds length and O–Ca–O and O–P–O bonds angle (**Figure 2**), which is a characteristic of ACP structure, originating the localized tail states (**Figure 4**). Besides, Bystrov *et al.* [54] evidenced by DFT calculations of HA that  $V_O$  vacancies in PO<sub>4</sub> groups lead to fully occupied peaks at 344 nm (3.60 eV eV), 358 nm (3.47 eV), and 366 nm (3.39 eV) below the CB. Huerta *et al.* [40] experimentally proposed that this level occurs at 373 nm (3.32 eV). In this study, we propose that the defect-related excitation band centered at 370 nm (3.35 eV) and 398 nm (3.10 eV) of ACP NPs mainly stems from energy states associated to  $V_O$  in PO<sub>4</sub><sup>3-</sup>. Hence, the PL emission (**Figure 5c**) originates by excited electrons departing from this band, which subsequently follow a complex multistep decay through radiative and non-radiative pathways involving distinct extended and/or localized levels. The latter levels could arise from tail states and from defect states due to  $V_O$  in PO<sub>4</sub><sup>3-</sup>,  $V_{Ca}$ , as well as from CO<sub>3</sub><sup>2-</sup> impurity and the defects associated to its stabilization in ACP lattice.

The heat treatment at 400 °C of ACP lead to a new excitation band in 400-520 nm range, which is closer to the excitation wavelength used (450 nm), rendering improved PL emissions compared to as-synthesized ACP NPs. We believe that this new band has a great contribution from temperature-induced changes of CO<sub>3</sub><sup>2-</sup> impurity trapped in ACP400 NPs and their environments. Zollfrank *et al.* [31] proposed that annealing biomimetic HA at 400 °C enhance the presence of self-trapped electrons in carbonates (CO<sub>3</sub><sup>2-</sup>) giving rise to improved PL emission. Our recent studies [36,49] with HA corroborated

by the investigations conducted by Gonzalez *et al.* [39] also concluded that  $\text{CO}_3^{2-}$  impurities could play important role on the PL emission observed in NPs heated at 350 – 450 °C. In the case of ACP structure, the SRO modifications in  $\text{CO}_3^{2-}$  group observed by FTIR spectrum of ACP400 NPs (**Figure 2b**) supports the aforementioned arguments, since (1) this group become richer in electronic density after annealing due to changes of interaction with surrounding crystal field, and (2)  $\text{CO}_3^{2-}$ -environment become more anisotropic (i.e., greater C–O bonds distortions). Hence, the changes in bond character of  $\text{CO}_3^{2-}$  group and in its surroundings, as well as the pronounced impact of the short-range disorder on  $\text{CO}_3^{2-}$  internal arrangement contribute to the improved excitation capability of ACP400 NPs in higher wavelengths regions than ACP NPs.

Furthermore, Zhang *et al.* [34] related the role of  $\text{CO}_2^{\cdot-}$  radicals for the PL observed in HA. Jiang *et al.* [10] more recently observed that these impurities are in fact N-rich carbon dots present on the surface and inside of HA NPs acting as luminescent centers, which was further corroborate by other studies [50,53]. However, no clear signs of carbon dots were observed herein. A main difference is that these authors used significant amounts of citrate precursors which is known to decompose in carbon dots by hydrothermal treatment. By XPS (section 3.3), we observed the presence of surface hydrocarbon chains adsorbed on the surface of ACP400 NPs. However, the substantial contribution of adventitious carbon to the PL emission can be discarded, since it is known that a similar adsorption capability is retained on the NPs after ACP→HA transition [106]. Nevertheless, as shown in **Figure 6b**, the emission intensity of HA400 is 5 times less intense compared to ACP400 NPs.

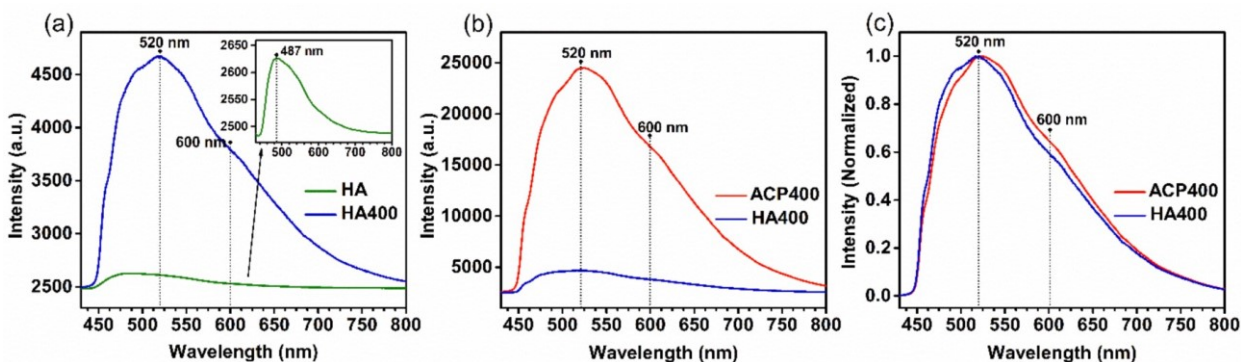


**Figure 6.** PL emission spectra ( $\lambda_{\text{exc}} = 405 \text{ nm}$ ) of (a) chemically precipitated HA obtained after ripening for 24 h and after conducting the heat treatment step at 400 °C, (b) PL spectra of ACP and HA heat treated at 400 °C, and (c) normalized PL spectra of ACP and HA heat treated at 400 °C.

Lattice water elimination when ACP is heat treated up to 400 °C is then a crucial mechanism to be considered to the improved PL properties of ACP400. Hydration water was previously proposed by Posner and Betts [65] to occupy interstitial positions between the  $\text{Ca}_9(\text{PO}_4)_6$  clusters composing the ACP NPs. Termine and Lundy [69] argued that  $\text{H}_2\text{O}$  molecules contribute with ACP coordination structure, and Du *et al.* [107] proposed that this water is coordinated with Ca atoms of the outer shell of Posner's subunits. Moreover, Uskoković *et al.* [61] stated that before annealing, the water-rich ACP lattice possesses a large amount of hydrogen bonding between  $\text{H}_2\text{O}$  molecules and  $\text{PO}_4^{3-}$  groups. Yasar *et al.*, [62] concluded by NMR measurements that there are close  $\text{H}_2\text{O}\cdots\text{CO}_3^{2-}$  and  $\text{H}_2\text{O}\cdots\text{PO}_4^{3-}$  contacts in the ACP-particle interior.

Due to this active bonding of  $\text{H}_2\text{O}$  molecules with their surroundings, it could be expected that their removal influences the bond character of the remaining atomic groups in ACP lattice, as was observed for the strong polarizable  $\text{PO}_4^{3-}$  and  $\text{CO}_3^{2-}$  groups. Moreover, as evidenced by Uskoković [60], an important shrinkage of the ACP lattice occurs by heating up to 400 °C in order to close the voids resultant from the release of water. This contraction with consequent increase in lattice strain and decrease in SRO of ACP400 lattice, observable as shifts and broadening of bands related to  $\text{PO}_4^{3-}$  and  $\text{CO}_3^{2-}$  vibrational modes in FTIR (**Figures 2d,f**), could intensify the electronic interactions between neighbor atomic groups with significant increase in PL emission intensity. This is because of the enhancement in oscillator strength and the consequent higher probability of radiative electronic transitions that takes place, as well as the increase in the density of localized states within the forbidden zone.

In our previous publication [36], we also observed an important contraction in crystalline lattice of HA NPs up to 400 °C/4h after the elimination of impurities with consequent increase in PL emission. This difference in PL intensity of ACP400 and HA400 materials could result mainly from the distinct characteristics of hydration water in their lattices. When the ACP→HA transition takes place in aqueous media, the concentration of hydration water is known to be reduced from ~15wt% for ACP to values below 3.5wt% for HA [49,67] and the activation energy ( $E_a$ ) for dehydration is also reduced from 23.6 kJ/mol for ACP to 12.5 kJ/mol for HA [61]. Thereby, ACP possess higher concentration of hydration water molecules which are more tightly bounded in its amorphous lattice than in HA one. These characteristics imply a less pronounced structural impact at short-range in HA lattice than in ACP by the loss of water, leading to lower density of similar localized energy states

and/or probability of radiative electronic transitions in HA400 NPs.

The experimental data obtained in this study evidenced that the heat treatment at intermediates temperatures close to 400 °C is an important step in order to obtain CaPs with improved PL properties. Pivotal role are the concomitant impurity reactions ( $\text{H}_2\text{O}$  and  $\text{CO}_3^{2-}$ ) that takes place in ACP lattice during the temperature-induced structural reorganization. These results could open venues toward new optical devices using ACP400 NPs with stable structural and PL properties, as demonstrated by the thermal stability probe (see section 3.1 and **Figure S3**) and the long-term stability analysis conducted after 10 months by collecting the FTIR and PL emission (**Figure S6**), where no significant changes were observed in comparison with the as-synthesized ACP400 sample.

#### 4.4.7. Cytotoxicity assay

The MTT assay was used to evaluate the cytotoxicity of ACP400 NPs on HDFn cells, and the results are illustrated in **Figure 7**. After incubation with ACP400 NPs for 24h and 48h, HDFn cells viability was superior to 95% in all NPs tested concentrations (from 20 to 320  $\mu\text{g}/\text{mL}$ ). The statistical analysis revealed that there is no significant difference between the control and APC400 NPs-treated cells, except for the ones containing 20  $\mu\text{g}/\text{mL}$  (24h), 40 and 80  $\mu\text{g}/\text{mL}$  (48h) of NPs, in which a slight increase in cell viability occurred. These results are in accordance with the superior cell viability found for luminescent HA NPs exposed to HDFn cells in similar conditions [49]. Hence, the low cytotoxicity observed for the luminescent ACP400 NPs evidences the potential of this CaP to be used as safe material for forensics purposes.

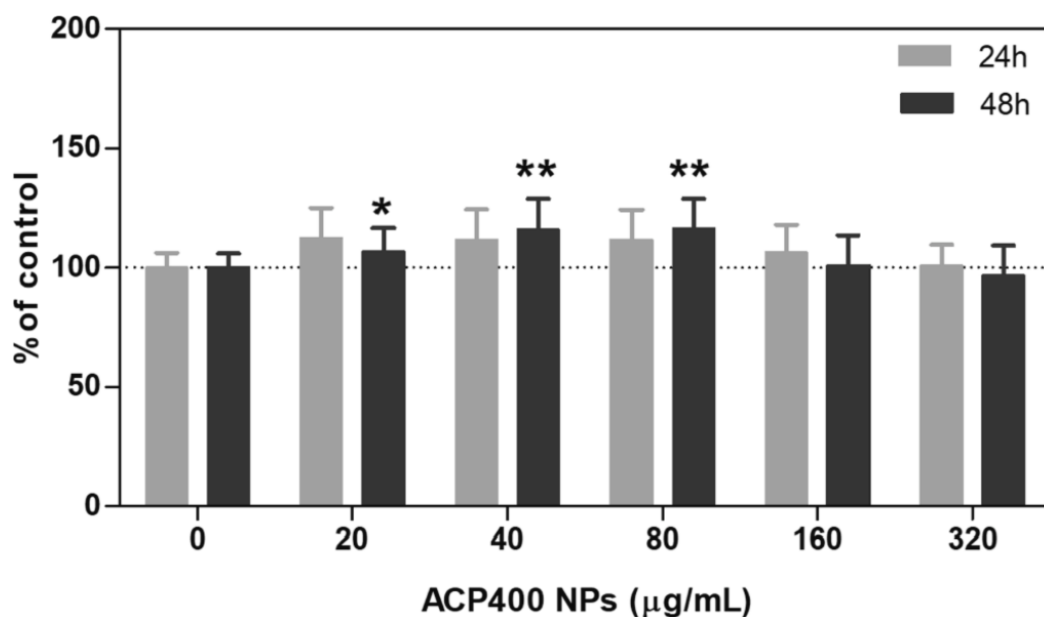


**Figure 7.** Cell viability analysis of HDFn cells after incubation with increasing concentrations of ACP400 NPs, for 24 and 48 h. Mean  $\pm$  SD of three independent experiments in triplicate. Asterisks indicate difference in comparison to the control (\* $p < 0.05$  and \*\* $p < 0.001$ ).

#### 4.4.8. Application for fingerprint imaging

The feasibility of ACP400 NP for fingerprint imaging was probed in a pair of surfaces from utensils of daily use, and the results are shown in **Figure 8**. Under UV light, the development of fingerprints was successfully obtained by the pale fluorescent yellow color from ACP400 NPs. Moreover, a more accurate image was observed in the stainless-steel tweezers (**Figure 8a**) than in the polymeric material on the screen smart surface (**Figure 8d**). This allowed us to obtain clear and well resolved ridges, bifurcations, and lakes.

To evaluate the viability of AC400 NPs as an alternative system for latent fingerprint imaging, the digitalized images obtained in the stainless-steel tweezers (**Figure 8b**) and in the polymeric material (**Figure 8e**) were compared with those acquired by the standard procedure in the entrance of the Police database based on ink fingerprints (**Figures 8c,f**). After the input on the Integrated Automated Fingerprint Identification System (IAFIS), a process using a computer to match fingerprints against a database of known fingerprints. Our analysis compared the different traits in the obtained fingerprint founding 14 matches. These results agree with the forensic requirements to be take in account for future legal actions.

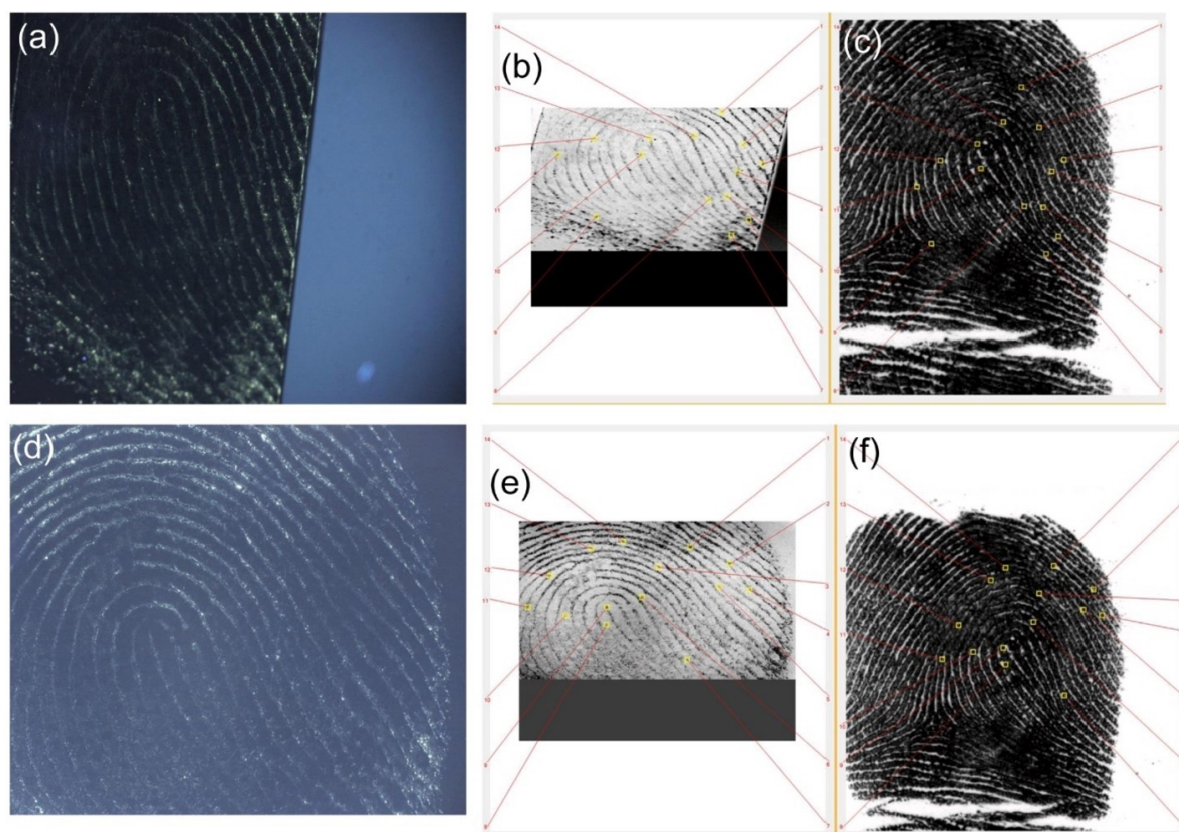


**Figure 8.** Latent fingerprint images based on ACP400 NPs obtained under UV irradiation in (a) tweezers and (d) LCD smartphone. (b,e) Digitalized images of UV-exposed surfaces containing ACP400 NPs. (c,f) Digitalized images of the fingerprints obtained from the standard procedure by ink processing. Data analysis was conducted using IAFIS system.

The mechanism for imaging fingerprints could be explained by the electrostatic interactions of the negative surface due to O=P–O functional groups (mainly phosphate) and basic proteins of the secretion components, as previously reported [86]. The analyst compares minutiae characteristics and locations to determine if they match. The analysis showed the satisfactory performance of ACP400 when used for latent fingerprint detection. ACP400 NPs are fluorescent and non-toxic, and the images obtained are more shiny than those obtained with ink. The proposed method offers a certain advantage to the methods that are currently used by the Scientific Police, such as those based on non fluorescent magnetic nanoparticles [113], dyes [8], ink [114], and metal oxides for fingerprint detection [115]. Furthermore, as highly fluorescent systems, it was previously proposed the application of QDs [12] but, due to their low biocompatibility, carbon dots were brought to light [22,24], and here we suggest the ACP400 NPs.



## 4.5. Conclusions

In summary, intrinsically photoluminescent, biocompatible, and stable nanoparticles based on chemically precipitated ACP heat-treated at 400 °C for 4 hours were successfully synthesized. SAED, XRD and FTIR results confirmed that the amorphous pattern was present after the heat treatment, but also stemmed a significant decrease in structural short-range ordering, observed in FTIR as a broadening of the  $\text{PO}_4^{3-}$  bands and an increase in peak asymmetry. Furthermore, the stereochemistry of the structural  $\text{CO}_3^{2-}$  groups present into the ACP amorphous lattice was also significantly affected. These structural changes occur due to the shrinkage of ACP lattice as an effect of hydration water elimination at 400 °C. The aforementioned phenomena, together with  $V_{\text{Ca}}$  and  $V_{\text{O}}$  vacancy in  $\text{PO}_4^{3-}$ , were attributed to be the possible causes of the high density of localized tail and defect states into the forbidden band gap of heat-treated ACP, detected by diffuse reflectance via UV-Vis spectroscopy, and by photoluminescence excitation and emission measurements. When excited at  $\lambda_{\text{exc}} = 450$  nm, the photoluminescence emission of heat-treated ACP nanoparticles is 50 times greater comparing to freshly precipitated ACP and consists of a broadband defect-related emission profile centered at 540 nm and encompassing most part of visible region (490 - 800 nm). The emission possesses a yellowish color, as was determined by CIE chromaticity coordinates using distinct excitation sources ( $x = 0.53$ ;  $y = 0.45$ , spectrofluorometer, and  $x = 0.52$ ;  $y = 0.44$ , HeCd laser). The structural and luminescent features remained almost unchanged after 10 months, demonstrating the superior stability of the heat-treated nanoparticles. When used for fingerprint imaging, the bright yellow patterns of unique features from ACP luminescence were well observed on the surface of tweezers and LCD smartphone under NUV irradiation ( $\lambda_{\text{exc}} = 450$  nm). These nanoparticles presented interactions with biomolecules and those interaction led to specific fluorescent patterns. Moreover, the non-cytotoxic response of ACP observed by MTT assay evidences the potential of this calcium orthophosphate to be used as safe material for forensics purposes.

## 4.6. Acknowledgments

The authors acknowledge the financial support of the following agencies: Conselho Nacional de Desenvolvimento Científico e Tecnológico (CNPq, Grants 164373/2020-9 and 141964/2018-9), and Fundação de Amparo à Pesquisa do Estado de São Paulo (FAPESP, Grant 2013/07296-2). MA thanks to COST Action 16101

and Spanish Ministry of Science and Innovation (project RTI2018-099668-B-C22). Special thanks to Prof. Andrea Simone Stucchi de Camargo Alvarez Bernardez and Dr. Leonnam Gotardo Merizio for the support with photoluminescence spectroscopy measurements and Prof. Waldir Avansi for the support with UV-Vis spectroscopy.

## 4.7. References

- [1] D.R. Ashbaugh, *Quantitative-qualitative friction ridge analysis: An introduction to basic and advanced ridgeology*, CRC Press, Boca Raton, Florida, 1999.
- [2] A.K. Jain, A. Ross, S. Prabhakar, An Introduction to Biometric Recognition, *IEEE Trans. Circuits Syst. Video Technol.* 14 (2004) 4–20, <https://doi.org/10.1109/TCSVT.2003.818349>.
- [3] D.A. Wilkinson, A. Misner, A comparison of thenoyl europium chelate with ardrox and rhodamine 6G for fluorescent detection of cyanoacrylate prints, *J. Forensic Identif.* 44 (1994) 387–407.
- [4] G. Sodhi, J. Kaur, R.K. Garg, Fingerprint powder formulations based on organic, fluorescent dyes, *J. Forensic Identif.* 54 (2004) 4–8.
- [5] D.S. Bhagat, P.B. Chavan, W.B. Gurnule, S.K. Shejul, I.V. Suryawanshi, Efficacy of synthesized azo dye for development of latent fingerprints on Non-porous and wet surfaces, *Mater. Today Proc.* 29 (2020) 1223–1228, <https://doi.org/10.1016/j.matpr.2020.05.480>.
- [6] H.L. Barros, L. Tavares, V. Stefani, Dye-doped starch microparticles as a novel fluorescent agent for the visualization of latent fingermarks on porous and non-porous substrates, *Forensic Chem.* 20 (2020), 100264, <https://doi.org/10.1016/j.forc.2020.100264>.
- [7] M. Chen, R. Chen, Y. Shi, J. Wang, Y. Cheng, Y. Li, X. Gao, Y. Yan, J.Z. Sun, A. Qin, R.T.K. Kwok, J.W.Y. Lam, B.Z. Tang, Malonitrile-Functionalized Tetraphenylpyrazine: Aggregation-Induced Emission, Ratiometric Detection of Hydrogen Sulfide, and Mechanochromism, *Adv. Funct. Mater.* 28 (2018) 1704689, <https://doi.org/10.1002/adfm.201704689>.
- [8] C. Yuan, M. Li, M. Wang, X. Zhang, Z. Yin, K. Song, Z. Zhang, Sensitive development of latent fingerprints using Rhodamine B-diatomaceous earth composites and principle of

efficient image enhancement behind their fluorescence characteristics, *Chem. Eng. J.* 383 (2020), 123076, [https://doi.org/ 10.1016/j.cej.2019.123076](https://doi.org/10.1016/j.cej.2019.123076).

[9] M.J. Choi, K.E. McBean, P.H.R. Ng, A.M. McDonagh, P.J. Maynard, C. Lennard, C. Roux, An evaluation of nanostructured zinc oxide as a fluorescent powder for fingerprint detection, *J. Mater. Sci.* 43 (2008) 732–737, <https://doi.org/10.1007/s10853-007-2178-5>.

[10] M. Algarra, J. Jiménez-Jiménez, R. Moreno-Tost, B.B. Campos, J.C.G. Esteves da Silva, CdS nanocomposites assembled in porous phosphate heterostructures for fingerprint detection, *Opt. Mater. (Amst)* 33 (2011) 893–898, <https://doi.org/10.1016/j.optmat.2011.01.017>.

[11] J. Dutta, S.A. Ramakrishna, I. Mekkaoui Alaoui, Fingerprint visualization enhancement by deposition of columnar thin films and fluorescent dye treatment, *Forensic Sci. Int.* 228 (1-3) (2013) 32–37.

[12] M. Algarra, K. Radotić, A. Kalauzi, D. Mutavdžić, A. Savić, J. Jiménez-Jiménez, E. Rodríguez-Castellón, J.C.G.E. da Silva, J.J. Guerrero-González, Fingerprint detection and using intercalated CdSe nanoparticles on non-porous surfaces, *Anal. Chim. Acta.* 812 (2014) 228–235, <https://doi.org/10.1016/j.aca.2014.01.015>.

[13] P. Wu, C. Xu, X. Hou, J.-J. Xu, H.-Y. Chen, Dual-emitting quantum dot nanohybrid for imaging of latent fingerprints: simultaneous identification of individuals and traffic light-type visualization of TNT, *Chem. Sci.* 6 (2015) 4445–4450, <https://doi.org/10.1039/C5SC01497B>.

[14] K. Cai, R. Yang, Y. Wang, X. Yu, J. Liu, Super fast detection of latent fingerprints with water soluble CdTe quantum dots, *Forensic Sci. Int.* 226 (2013) 240–243, <https://doi.org/10.1016/j.forsciint.2013.01.035>.

[15] J. Liu, Z. Shi, Y. Yu, R. Yang, S. Zuo, Water-soluble multicolored fluorescent CdTe quantum dots: Synthesis and application for fingerprint developing, *J. Colloid Interface Sci.* 342 (2010) 278–282, <https://doi.org/10.1016/j.jcis.2009.10.061>.

[16] M. Wang, M. Li, A. Yu, J. Wu, C. Mao, Rare Earth Fluorescent Nanomaterials for Enhanced Development of Latent Fingerprints, *ACS Appl. Mater. Interfaces.* 7 (2015) 28110–28115, <https://doi.org/10.1021/acsami.5b09320>.

[17] N.M. Maalej, A. Qurashi, I. Bennour, L.R. Haddada, M.N. Shaikh, M. Ilyas, N. Essoukri

Ben Amara, R. Maalej, M.A. Gondal, Green Emitting Rare Earth Gd<sub>2</sub>O<sub>3</sub>: Tb<sup>3+</sup> Nanoparticles for Rapid Imaging of Latent Fingerprint, *Methods Appl. Fluoresc.* 9 (2021) 025002.  
<https://doi.org/10.1088/2050-6120/abdbc0>.

[18] X. Wang, L. Yan, S. Liu, P. Zhang, R. Huang, B. Zhou, Enhancing energy migration upconversion through a migratory interlayer in the core–shell–shell nanostructure towards latent fingerprinting, *Nanoscale.* 12 (2020) 18807–18814,  
<https://doi.org/10.1039/D0NR03817B>.

[19] Y. Yang, X. Liu, Y. Lu, L. Tang, J. Zhang, L. Ge, F. Li, Visualization of latent fingerprints using a simple “silver imaging ink”, *Anal. Methods.* 8 (2016) 6293–6297,  
<https://doi.org/10.1039/C6AY01811D>.

[20] Y.-H. Cheng, Y. Zhang, S.-L. Chau, S.-K.-M. Lai, H.-W. Tang, K.-M. Ng, Enhancement of Image Contrast, Stability, and SALDI-MS Detection Sensitivity for Latent Fingerprint Analysis by Tuning the Composition of Silver-Gold Nanoalloys, *ACS Appl. Mater. Interfaces.* 8 (2016) 29668–29675, <https://doi.org/10.1021/acsami.6b09668>.

[21] G. Kolhatkar, C. Parisien, A. Ruediger, C. Muehlethaler, Latent Fingerprint Imaging by Single-Metal Deposition of Gold Nanoparticles and Surface Enhanced Raman Spectroscopy, *Front. Chem.* 7 (2019) 440, <https://doi.org/10.3389/fchem.2019.00440>.

[22] I. Milenkovic, M. Algarra, C. Alcoholado, M. Cifuentes, J.M. Lázaro-Martínez, E. Rodríguez-Castellón, D. Mutavdžić, K. Radotić, T.J. Bandosz, Fingerprint imaging using N-doped carbon dots, *Carbon N. Y.* 144 (2019) 791–797, <https://doi.org/10.1016/j.carbon.2018.12.102>.

[23] D. Fernandes, M.J. Krysmann, A. Kellarakis, Carbogenically coated silica nanoparticles and their forensic applications, *Chem. Commun.* 52 (2016) 8294–8296,  
<https://doi.org/10.1039/C6CC02556K>.

[24] M. Algarra, D. Bartolić, K. Radotić, D. Mutavdžić, M.S. Pino-González, E. Rodríguez-Castellón, J.M. Lázaro-Martínez, J.J. Guerrero-González, J. C. Esteves da Silva, J. Jiménez-Jiménez, P-doped carbon nano-powders for fingerprint imaging, *Talanta* 194 (2019) 150–157,  
<https://doi.org/10.1016/j.talanta.2018.10.033>.

[25] E. Prabakaran, K. Pillay, Synthesis and characterization of fluorescent N-CDs/ ZnONPs nanocomposite for latent fingerprint detection by using powder brushing method, *Arab. J.*

Chem. 13 (2020) 3817–3835, <https://doi.org/10.1016/j.arabjc.2019.01.004>.

[26] F. Wang, W.B. Tan, Y. Zhang, X. Fan, M. Wang, Luminescent nanomaterials for biological labelling, *Nanotechnology*. 17 (2006) R1–R13, <https://doi.org/10.1088/0957-4484/17/1/R01>.

[27] M. Vallet-Regí, J.M. González-Calbet, Calcium phosphates as substitution of bone tissues, *Prog. Solid State Chem.* 32 (2004) 1–31, <https://doi.org/10.1016/j.progsolidstchem.2004.07.001>.

[28] K. Lin, C. Wu, J. Chang, Advances in synthesis of calcium phosphate crystals with controlled size and shape, *Acta Biomater.* 10 (2014) 4071–4102, <https://doi.org/10.1016/j.actbio.2014.06.017>.

[29] C. Qi, J. Lin, L.H. Fu, P. Huang, Calcium-based biomaterials for diagnosis, treatment, and theranostics, *Chem. Soc. Rev.* 47 (2018) 357–403, <https://doi.org/10.1039/c6cs00746e>.

[30] S.S. Syamchand, G. Sony, Multifunctional hydroxyapatite nanoparticles for drug delivery and multimodal molecular imaging, *Microchim. Acta.* 182 (2015) 1567–1589, <https://doi.org/10.1007/s00604-015-1504-x>.

[31] C. Zollfrank, L. Müller, P. Greil, F.A. Müller, Photoluminescence of annealed biomimetic apatites, *Acta Biomater.* 1 (2005) 663–669, <https://doi.org/10.1016/j.actbio.2005.06.004>.

[32] D. Aronov, A. Karlov, G. Rosenman, Hydroxyapatite nanoceramics: Basic physical properties and biointerface modification, *J. Eur. Ceram. Soc.* 27 (2007) 4181–4186, <https://doi.org/10.1016/j.jeurceramsoc.2007.02.121>.

[33] D. Aronov, M. Chaikina, J. Haddad, A. Karlov, G. Mezinskis, L. Oster, I. Pavlovska, G. Rosenman, Electronic states spectroscopy of Hydroxyapatite ceramics, *J. Mater. Sci. Mater. Med.* 18 (2007) 865–870, <https://doi.org/10.1007/s10856-006-0080-3>.

[34] C. Zhang, J. Yang, Z. Quan, P. Yang, C. Li, Z. Hou, J. Lin, Hydroxyapatite nano- and microcrystals with multiform morphologies: Controllable synthesis and luminescence properties, *Cryst. Growth Des.* 9 (2009) 2725–2733, <https://doi.org/10.1021/cg801353n>.

[35] A.V. Bystrova, Y.D. Dekhtyar, A.I. Popov, J. Coutinho, V.S. Bystrov, Modified

hydroxyapatite structure and properties: Modeling and synchrotron data analysis of modified hydroxyapatite structure, *Ferroelectrics* 475 (2015) 135–147, <https://doi.org/10.1080/00150193.2015.995580>.

[36] T.R. Machado, J.C. Sczancoski, H. Beltrán-Mir, I.C. Nogueira, M.S. Li, J. Andrés, E. Cordoncillo, E. Longo, A novel approach to obtain highly intense self-activated photoluminescence emissions in hydroxyapatite nanoparticles, *J. Solid State Chem.* 249 (2017) 64–69, <https://doi.org/10.1016/j.jssc.2016.12.018>.

[37] T.R. Machado, J.C. Sczancoski, H. Beltrán-Mir, M.S. Li, J. Andrés, E. Cordoncillo, E. Leite, E. Longo, Structural properties and self-activated photoluminescence emissions in hydroxyapatite with distinct particle shapes, *Ceram. Int.* 44 (2018) 236–245, <https://doi.org/10.1016/j.ceramint.2017.09.164>.

[38] D.L. Goloshchapov, P.V. Seredin, D.A. Minakov, E.P. Domashevskaya, Photoluminescence Properties of Nanoporous Nanocrystalline Carbonate- Substituted Hydroxyapatite, *Opt. Spectrosc. (English Transl. Opt. i Spektrosk.* 124 (2018) 187–192, <https://doi.org/10.1134/S0030400X18020066>.

[39] G. Gonzalez, C. Costa-Vera, L.J. Borrero, D. Soto, L. Lozada, J.I. Chango, J.C. Diaz, L. Lascano, Effect of carbonates on hydroxyapatite self-activated photoluminescence response, *J. Lumin.* 195 (2018) 385–395, <https://doi.org/10.1016/j.jlumin.2017.11.058>.

[40] V.J. Huerta, P. Fernández, V. Gómez, O.A. Graeve, M. Herrera, Defect-related luminescence properties of hydroxyapatite nanobelts, *Appl. Mater. Today.* 21 (2020), 100822, <https://doi.org/10.1016/j.apmt.2020.100822>.

[41] E.X. Figueroa-Rosales, J. Martínez-Juárez, E. García-Díaz, D. Hernández-Cruz, S. A. Sabinas-Hernández, M.J. Robles-Águila, Photoluminescent properties of hydroxyapatite and hydroxyapatite/multi-walled carbon nanotube composites, *Crystals.* 11 (2021) 832, <https://doi.org/10.3390/cryst11070832>.

[42] A. Sinha, A. Pal, A. Santra, S. Murmu, U.K. Ghorai, A.R. Chowdhury, D. Banerjee, Calcination Temperature-Dependent Structural and Photoluminescence Properties of Hydroxyapatite Derived from Labeo Rohita Fish Scales, *J. Inst. Eng. Ser. D.* 101 (2) (2020) 223–232.

[43] C. Zhang, C. Li, S. Huang, Z. Hou, Z. Cheng, P. Yang, C. Peng, J. Lin, Self-activated

luminescent and mesoporous strontium hydroxyapatite nanorods for drug delivery, *Biomaterials* 31 (2010) 3374–3383, <https://doi.org/10.1016/j.biomaterials.2010.01.044>.

[44] Z. Li, Z. Liu, M. Yin, X. Yang, Q. Yuan, J. Ren, X. Qu, Aptamer-capped multifunctional mesoporous strontium hydroxyapatite nanovehicle for cancer-cell-responsive drug delivery and imaging, *Biomacromolecules* 13 (2012) 4257–4263, <https://doi.org/10.1021/bm301563q>.

[45] G.S. Kumar, E.K. Girija, Flower-like hydroxyapatite nanostructure obtained from eggshell: A candidate for biomedical applications, *Ceram. Int.* 39 (2013) 8293–8299, <https://doi.org/10.1016/j.ceramint.2013.03.099>.

[46] R.K. Singh, T.H. Kim, K.D. Patel, J.J. Kim, H.W. Kim, Development of biocompatible apatite nanorod-based drug-delivery system with in situ fluorescence imaging capacity, *J. Mater. Chem. B.* 2 (2014) 2039–2050, <https://doi.org/10.1039/c3tb21156h>.

[47] S.Y. Park, K. Il Kim, S.P. Park, J.H. Lee, H.S. Jung, Aspartic Acid-Assisted Synthesis of Multifunctional Strontium-Substituted Hydroxyapatite Microspheres, *Cryst. Growth Des.* 16 (2016) 4318–4326, <https://doi.org/10.1021/acs.cgd.6b00420>.

[48] K. Deshmukh, M.M. Shaik, S.R. Ramanan, M. Kowshik, Self-Activated Fluorescent Hydroxyapatite Nanoparticles: A Promising Agent for Bioimaging and Biolabeling, *ACS Biomater. Sci. Eng.* 2 (2016) 1257–1264, <https://doi.org/10.1021/acsbiomaterials.6b00169>.

[49] T.R. Machado, I.S. Leite, N.M. Inada, M.S. Li, J.S. da Silva, J. Andrés, H. Beltrán- Mir, E. Cordoncillo, E. Longo, Designing biocompatible and multicolor fluorescent hydroxyapatite nanoparticles for cell-imaging applications, *Mater. Today Chem.* 14 (2019), 100211, <https://doi.org/10.1016/j.mtchem.2019.100211>.

[50] C. Wang, K.-J. Jeong, J. Kim, S.W. Kang, J. Kang, I.H. Han, I.-W. Lee, S.-J. Oh, J. Lee, Emission-tunable probes using terbium(III)-doped self-activated luminescent hydroxyapatite for in vitro bioimaging, *J. Colloid Interface Sci.* 581 (2021) 21–30, <https://doi.org/10.1016/j.jcis.2020.07.083>.

[51] K. Zhang, K. Zeng, C. Shen, S. Tian, M. Yang, Determination of protein kinase A activity and inhibition by using hydroxyapatite nanoparticles as a fluorescent probe, *Microchim. Acta.* 185 (2018), <https://doi.org/10.1007/s00604-018-2754-1>.

[52] W. Yang, J. Luo, M. Qi, M. Yang, Detection of alkaline phosphatase activity and

inhibition with fluorescent hydroxyapatite nanoparticles, *Anal. Methods*. 11 (2019) 2272–2276, <https://doi.org/10.1039/c9ay00176j>.

[53] C. Cheng, K. Tong, Y. Fang, J. Wang, Y. Liu, J. Tan, Ammonium-induced synthesis of highly fluorescent hydroxyapatite nanoparticles with excellent aqueous colloidal stability for secure information storage, *Coatings*. 9 (2019) 1–14, <https://doi.org/10.3390/coatings9050289>.

[54] V.S. Bystrov, C. Piccirillo, D.M. Tobaldi, P.M.L. Castro, J. Coutinho, S. Kopyl, R. C. Pullar, Oxygen vacancies, the optical band gap ( $E_g$ ) and photocatalysis of hydroxyapatite: Comparing modelling with measured data, *Appl. Catal. B Environ.* 196 (2016) 100–107, <https://doi.org/10.1016/j.apcatb.2016.05.014>.

[55] G. Lambrecht, C. Mallol, Autofluorescence of experimentally heated bone: Potential archaeological applications and relevance for estimating degree of burning, *J. Archaeol. Sci. Reports*. 31 (2020), 102333, <https://doi.org/10.1016/j.jasrep.2020.102333>.

[56] A. Sandri, P.R. Basso, I. Corridori, M. Protasoni, G. Segalla, M. Raspanti, A. E. Spinelli, F. Boschi, Photon emission and changes in fluorescent properties of bone after laser irradiation, *J. Biophotonics*. 14 (2021) 1–9, <https://doi.org/10.1002/jbio.202000445>.

[57] D.L. Goloshchapov, D.A. Minakov, E.P. Domashevskaya, P.V. Seredin, Excitation of luminescence of the nanoporous bioactive nanocrystalline carbonate-substituted hydroxyapatite for early tooth disease detection, *Results Phys.* 7 (2017) 3853–3858, <https://doi.org/10.1016/j.rinp.2017.09.055>.

[58] S.V. Dorozhkin, Amorphous calcium (ortho)phosphates, *Acta Biomater.* 6 (2010) 4457–4475, <https://doi.org/10.1016/j.actbio.2010.06.031>.

[59] C. Combes, C. Rey, Amorphous calcium phosphates: Synthesis, properties and uses in biomaterials, *Acta Biomater.* 6 (2010) 3362–3378, <https://doi.org/10.1016/j.actbio.2010.02.017>.

[60] V. Uskoković, Disordering the Disorder as the Route to a Higher Order: Incoherent Crystallization of Calcium Phosphate through Amorphous Precursors, *Cryst. Growth Des.* 19 (2019) 4340–4357, <https://doi.org/10.1021/acs.cgd.9b00061>.

[61] V. Uskoković, S. Marković, L. Veselinović, S. Škapin, N. Ignjatović, D.P. Uskoković,



Insights into the kinetics of thermally induced crystallization of amorphous calcium phosphate, *Phys. Chem. Chem. Phys.* 20 (2018) 29221–29235, <https://doi.org/10.1039/c8cp06460a>.

[62] O.F. Yasar, W.C. Liao, B. Stevansson, M. Edén, Structural Role and Spatial Distribution of Carbonate Ions in Amorphous Calcium Phosphate, *J. Phys. Chem. C.* 125 (2021) 4675–4693, <https://doi.org/10.1021/acs.jpcc.0c10355>.

[63] M. Edén, Structure and formation of amorphous calcium phosphate and its role as surface layer of nanocrystalline apatite: Implications for bone mineralization, *Materialia.* 17 (2021), 101107, <https://doi.org/10.1016/j.mtla.2021.101107>.

[64] S.V. Dorozhkin, Synthetic amorphous calcium phosphates (ACPs): Preparation, structure, properties, and biomedical applications, *Biomater. Sci.* 9 (2021) 7748–7798, <https://doi.org/10.1039/d1bm01239h>.

[65] A.S. Posner, F. Betts, Synthetic Amorphous Calcium Phosphate and Its Relation to Bone Mineral Structure, *Acc. Chem. Res.* 8 (8) (1975) 273–281.

[66] S. Somrani, M. Banu, M. Jemal, C. Rey, Physico-chemical and thermochemical studies of the hydrolytic conversion of amorphous tricalcium phosphate into apatite, *J. Solid State Chem.* 178 (2005) 1337–1348, <https://doi.org/10.1016/j.jssc.2004.11.029>.

[67] E.D. Eanes, Thermochemical studies on amorphous calcium phosphate, *Calcif. Tissue Res.* 5 (1970) 133–145, <https://doi.org/10.1007/BF02017543>.

[68] N. Li, W. Cui, P. Cong, J. Tang, Y. Guan, C. Huang, Y. Liu, C. Yu, R. Yang, X. Zhang, Biomimetic inorganic-organic hybrid nanoparticles from magnesium-substituted amorphous calcium phosphate clusters and polyacrylic acid molecules, *Bioact. Mater.* 6 (2021) 2303–2314, <https://doi.org/10.1016/j.bioactmat.2021.01.005>.

[69] J.D. Termine, D.R. Lundy, Vibrational spectra of some phosphate salts amorphous to X-ray diffraction, *Calcif. Tissue Res.* 15 (1974) 55–70, <https://doi.org/10.1007/BF02059043>.

[70] S.J. Gadaleta, E.P. Paschalis, F. Betts, R. Mendelsohn, A.L. Boskey, Fourier transform infrared spectroscopy of the solution-mediated conversion of amorphous calcium phosphate to hydroxyapatite: New correlations between X-ray diffraction and infrared data, *Calcif. Tissue Int.* 58 (1996) 9–16, <https://doi.org/10.1007/BF02509540>.

- [71] D. Tadic, F. Peters, M. Epple, Continuous synthesis of amorphous carbonated apatites, *Biomaterials* 23 (2002) 2553–2559, [https://doi.org/10.1016/S0142-9612\(01\)00390-8](https://doi.org/10.1016/S0142-9612(01)00390-8).
- [72] P. Layrolle, A. Lebugle, Characterization and Reactivity of Nanosized Calcium Phosphates Prepared in Anhydrous Ethanol, *Chem. Mater.* 6 (1994) 1996–2004, <https://doi.org/10.1021/cm00047a019>.
- [73] J. Vecstaudza, M. Gasik, J. Locs, Amorphous calcium phosphate materials: Formation, structure and thermal behaviour, *J. Eur. Ceram. Soc.* 39 (2019) 1642–1649, <https://doi.org/10.1016/j.jeurceramsoc.2018.11.003>.
- [74] P.C.H. Mitchell, S.F. Parker, K. Simkiss, J. Simmons, M.G. Taylor, Hydrated sites in biogenic amorphous calcium phosphates: An infrared, Raman, and inelastic neutron scattering study, *J. Inorg. Biochem.* 62 (1996) 183–197, [https://doi.org/10.1016/0162-0134\(95\)00146-8](https://doi.org/10.1016/0162-0134(95)00146-8).
- [75] J.M. Holmes, R.A. Beebe, Surface areas by gas adsorption on amorphous calcium phosphate and crystalline hydroxyapatite, *Calcif. Tissue Res.* 7 (1971) 163–174, <https://doi.org/10.1007/BF02062604>.
- [76] J.D. Termine, E.D. Eanes, Comparative chemistry of amorphous and apatitic calcium phosphate preparations, *Calcif. Tissue Res.* 10 (1972) 171–197, <https://doi.org/10.1007/BF02012548>.
- [77] G. Montes-Hernandez, F. Renard, Nucleation of Brushite and Hydroxyapatite from Amorphous Calcium Phosphate Phases Revealed by Dynamic in Situ Raman Spectroscopy, *J. Phys. Chem. C.* 124 (2020) 15302–15311, <https://doi.org/10.1021/acs.jpcc.0c04028>.
- [78] M. Fleet, *Carbonated hydroxyapatite: Materials, synthesis, and applications* (2014).
- [79] T. Theophanides, *Infrared spectroscopy - Materials Science, Eng. Technol.* (2012).
- [80] D. Stoilova, V. Koleva, V. Vassileva, Infrared study of some synthetic phases of malachite ( $\text{Cu}_2(\text{OH})_2\text{CO}_3$ )-hydrozincite ( $\text{Zn}_5(\text{OH})_6(\text{CO}_3)_2$ ) series, *Spectrochim. Acta - Part A Mol, Biomol. Spectrosc.* 58 (9) (2002) 2051–2059.
- [81] J.E. Amonette, D. Rai, Identification of noncrystalline (Fe, Cr)(OH)<sub>3</sub> by infrared spectroscopy, *Clays Clay Miner.* 38 (1990) 129–136.
- [82] J.P. Jolivet, Y. Thomas, B. Tavel, V. Lorenzelli, G. Busca, Infrared spectra of cerium

and thorium pentacarbonate complexes, *J. Mol. Struct.* 79 (1982) 403–408,  
[https://doi.org/10.1016/0022-2860\(82\)85091-6](https://doi.org/10.1016/0022-2860(82)85091-6).

[83] J.F. Moulder, W.F. Stickle, P.E. Sobol, K.D. Bomben, *Handbook of X-ray photoelectron spectroscopy: A reference book of standard spectra for identification and interpretation of XPS, Data* (1995).

[84] V. Bemmer, M. Bowker, J.H. Carter, P.R. Davies, L.E. Edwards, K.D.M. Harris, C. E. Hughes, F. Robinson, D.J. Morgan, M.G. Thomas, Rationalization of the X-ray photoelectron spectroscopy of aluminium phosphates synthesized from different precursors, *RSC Adv.* 10 (14) (2020) 8444–8452.

[85] S. Kasap, P. Capper, *Springer handbook of electronic and photonic materials*, 2<sup>nd</sup> edition, Springer International Publishing, Gewerbestrasse, Switzerland, 2017.  
[https://doi.org/10.1007/978-3-319-48933-9\\_39](https://doi.org/10.1007/978-3-319-48933-9_39).

[86] Z. Chen, H.N. Dinh, E. Miller, *Photoelectrochemical Water Splitting: Standards, Experimental Methodos, and Protocols*, Springer-Verlag, New York (2013),  
<https://doi.org/10.1016/B978-0-12-814134-2.00028-0>.

[87] P. Makuła, M. Pacia, W. Macyk, How To Correctly Determine the Band Gap Energy of Modified Semiconductor Photocatalysts Based on UV-Vis Spectra, *J. Phys. Chem. Lett.* 9 (2018) 6814–6817, <https://doi.org/10.1021/acs.jpcclett.8b02892>.

[88] L. Liang, P. Rulis, W.Y. Ching, Mechanical properties, electronic structure and bonding of  $\alpha$ - and  $\beta$ -tricalcium phosphates with surface characterization, *Acta Biomater.* 6 (2010) 3763–3771, <https://doi.org/10.1016/j.actbio.2010.03.033>.

[89] P. Rulis, L. Ouyang, W.Y. Ching, Electronic structure and bonding in calcium apatite crystals: Hydroxyapatite, fluorapatite, chlorapatite, and bromapatite, *Phys. Rev. B - Condens. Matter Mater. Phys.* 70 (2004) 1–8, <https://doi.org/10.1103/PhysRevB.70.155104>.

[90] A. Slepko, A.A. Demkov, First-principles study of the biomineral hydroxyapatite, *Phys. Rev. B - Condens. Matter Mater. Phys.* 84 (2011) 1–11, <https://doi.org/10.1103/PhysRevB.84.134108>.

[91] M.E. Zilm, L. Chen, V. Sharma, A. McDannald, M. Jain, R. Ramprasad, M. Wei, Hydroxyapatite substituted by transition metals: Experiment and theory, *Phys. Chem. Chem.*

Phys. 18 (2016) 16457–16465, <https://doi.org/10.1039/c6cp00474a>.

[92] Y. Jiménez-Flores, M. Suárez-Quezada, J.B. Rojas-Trigos, L. Lartundo-Rojas, V. Suárez, A. Mantilla, Characterization of Tb-doped hydroxyapatite for biomedical applications: optical properties and energy band gap determination, *J. Mater. Sci.* 52 (2017) 9990–10000, <https://doi.org/10.1007/s10853-017-1201-8>.

[93] N.L. Ignjatović, L. Mančić, M. Vuković, Z. Stojanović, M.G. Nikolić, S. Škapin, S. Jovanović, L. Veselinović, V. Uskoković, S. Lazić, S. Marković, M.M. Lazarević, D.P. Uskoković, Rare-earth ( $Gd^{3+}$ ,  $Yb^{3+}/Tm^{3+}$ ,  $Eu^{3+}$ ) co-doped hydroxyapatite as magnetic, up-conversion and down-conversion materials for multimodal imaging, *Sci. Rep.* 9 (2019) 1–15, <https://doi.org/10.1038/s41598-019-52885-0>.

[94] S.S. Bhat, U.V. Waghmare, U. Ramamurty, First-principles study of structure, vibrational, and elastic properties of stoichiometric and calcium-deficient hydroxyapatite, *Cryst. Growth Des.* 14 (2014) 3131–3141, <https://doi.org/10.1021/cg5004269>.

[95] B. Goswami, A. Choudhury, Enhanced visible luminescence and modification in morphological properties of cadmium oxide nanoparticles induced by annealing, *J. Exp. Nanosci.* 10 (2015) 900–910, <https://doi.org/10.1080/17458080.2014.933492>.

[96] E. Cerrato, M.C. Paganini, E. Giamello, Photoactivity under visible light of defective ZnO investigated by EPR spectroscopy and photoluminescence, *J. Photochem. Photobiol. A Chem.* 397 (2020), 112531, <https://doi.org/10.1016/j.jphotochem.2020.112531>.

[97] E.R. Leite, F.M. Pontes, E.C. Paris, C.A. Paskocimas, E.J.H. Lee, E. Longo, P. S. Pizani, J.A. Varela, V. Mastelaro, Amorphous lead titanate: A new wide-band gap semiconductor with photoluminescence at room temperature, *Adv. Funct. Mater.* 10 (2000) 235–240, [https://doi.org/10.1002/1099-0712\(200011/12\)10:6<235::AID-AMO409>3.0.CO;2-6](https://doi.org/10.1002/1099-0712(200011/12)10:6<235::AID-AMO409>3.0.CO;2-6).

[98] E. Orhan, M. Anicete-Santos, M.A.M.A. Maurera, F.M. Pontes, C.O. Paiva-Santos, A.G. Souza, J.A. Varela, P.S. Pizani, E. Longo, Conditions giving rise to intense visible room temperature photoluminescence in  $SrWO_4$  thin films: The role of disorder, *Chem. Phys.* 312 (2005) 1–9, <https://doi.org/10.1016/j.chemphys.2004.11.013>.

[99] M. Anicete-Santos, M.S. Silva, E. Orhan, M.S. Góes, M.A. Zaghete, C.O. Paiva-Santos, P.S. Pizani, M. Cilense, J.A. Varela, E. Longo, Contribution of structural order-disorder to the room-temperature photoluminescence of lead zirconate titanate powders, *J. Lumin.* 127

(2007) 689–695, <https://doi.org/10.1016/j.jlumin.2007.04.002>.

[100] V. Uskoković, D.P. Uskoković, Nanosized hydroxyapatite and other calcium phosphates: Chemistry of formation and application as drug and gene delivery agents, *J. Biomed. Mater. Res.* 96B (1) (2011) 152–191.

[101] K. Onuma, A. Ito, Cluster Growth Model for Hydroxyapatite, *Chem. Mater.* 10 (1998) 3346–3351, <https://doi.org/10.1021/cm980062c>.

[102] A. Lotsari, A.K. Rajasekharan, M. Halvarsson, M. Andersson, Transformation of amorphous calcium phosphate to bone-like apatite, *Nat. Commun.* 9 (2018) 4170, <https://doi.org/10.1038/s41467-018-06570-x>.

[103] K. Matsunaga, A. Kuwabara, First-principles study of vacancy formation in hydroxyapatite, *Phys. Rev. B - Condens. Matter Mater. Phys.* 75 (2007) 1–9, <https://doi.org/10.1103/PhysRevB.75.014102>.

[104] V.S. Bystrov, J. Coutinho, A.V. Bystrova, Y.D. Dekhtyar, R.C. Pullar, A. Poronin, E. Palcevskis, A. Dindune, B. Alkan, C. Durucan, E.V. Paramonova, Computational study of hydroxyapatite structures, properties and defects, *J. Phys. D. Appl. Phys.* 48 (19) (2015) 195302.

[105] D. Jiang, H. Zhao, Y. Yang, Y. Zhu, X. Chen, J. Sun, K. Yu, H. Fan, X. Zhang, Investigation of luminescent mechanism: N-rich carbon dots as luminescence centers in fluorescent hydroxyapatite prepared using a typical hydrothermal process, *J. Mater. Chem. B.* 5 (2017) 3749–3757, <https://doi.org/10.1039/c6tb03184f>.

[106] V. Uskoković, X-ray photoelectron and ion scattering spectroscopic surface analyses of amorphous and crystalline calcium phosphate nanoparticles with different chemical histories, *Phys. Chem. Chem. Phys.* 22 (2020) 5531–5547, <https://doi.org/10.1039/c9cp06529f>.

[107] L.W. Du, S. Bian, B. Di Gou, Y. Jiang, J. Huang, Y.X. Gao, Y.D. Zhao, W. Wen, T. L. Zhang, K. Wang, Structure of clusters and formation of amorphous calcium phosphate and hydroxyapatite: From the perspective of coordination chemistry, *Cryst. Growth Des.* 13 (2013) 3103–3109, <https://doi.org/10.1021/cg400498j>.

[108] P. Yang, Z. Quan, C. Li, X. Kang, H. Lian, J. Lin, Bioactive, luminescent and mesoporous europium-doped hydroxyapatite as a drug carrier, *Biomaterials* 29 (2008) 4341–

4347, <https://doi.org/10.1016/j.biomaterials.2008.07.042>.

[109] J. Hui, X. Zhang, Z. Zhang, S. Wang, L. Tao, Y. Wei, X. Wang, Fluoridated HAp:Ln<sup>3+</sup> (Ln = Eu or Tb) nanoparticles for cell-imaging, *Nanoscale*. 4 (2012) 6967–6970, <https://doi.org/10.1039/c2nr32404k>.

[110] Y. Xie, W. He, F. Li, T.S.H. Perera, L. Gan, Y. Han, X. Wang, S. Li, H. Dai, Luminescence Enhanced Eu<sup>3+</sup>/Gd<sup>3+</sup> Co-Doped Hydroxyapatite Nanocrystals as Imaging Agents in Vitro and in Vivo, *ACS Appl. Mater. Interfaces*. 8 (2016) 10212–10219, <https://doi.org/10.1021/acsami.6b01814>.

[111] H.N. Van, P.D. Tam, N.D.T. Kien, P.T. Huy, V.-H. Pham, Enhancing the luminescence of Eu<sup>3+</sup> /Eu<sup>2+</sup> ion-doped hydroxyapatite by fluoridation and thermal annealing : fluor-hydroxyapatite; luminescence; europium, nanobiophosphors, *Luminescence* 32 (5) (2017) 817–823.

[112] K. Carrera, V. Huerta, V. Orozco, J. Matutes, P. Fernández, O.A. Graeve, M. Herrera, Formation of vacancy point-defects in hydroxyapatite nanobelts by selective incorporation of Fe<sup>3+</sup> ions in Ca (II) sites. A CL and XPS study, *Mater. Sci. Eng. B Solid-State Mater. Adv. Technol.* 271 (2021) 115308.

[113] S.S. Nadar, R.K. Kelkar, P.V. Pise, N.P. Patil, S.P. Patil, N.S. Chaubal-Durve, V. P. Bhange, M.S. Tiwari, P.D. Patil, The untapped potential of magnetic nanoparticles for forensic investigations: A comprehensive review, *Talanta* 230 (2021), 122297, <https://doi.org/10.1016/j.talanta.2021.122297>.

[114] N. Attard Montalto, J.J. Ojeda, B.J. Jones, Determining the order of deposition of natural latent fingerprints and laser printed ink using chemical mapping with secondary ion mass spectrometry, *Sci. Justice*. 53 (2013) 2–7, <https://doi.org/10.1016/j.scijus.2012.05.007>.

[115] M.W. Mofulatsi, E. Prabakaran, T. Velempini, E. Green, K. Pillay, Preparation of manganese oxide coated coal fly ash adsorbent for the removal of lead and reuse for latent fingerprint detection, *Microporous Mesoporous Mater.*

## 4.8. Supplementary material

### **Amorphous Calcium Phosphate Nanoparticles Allow Fingerprint Detection via Self-Activated Luminescence**

Thales R. Machado,<sup>a,b,\*</sup> Jussara S. da Silva,<sup>b</sup> Renata R. Miranda,<sup>a</sup> Valtencir Zucolotto,<sup>a</sup> Máximo S. Li,<sup>c</sup> Maria V.M. de Yuso,<sup>d</sup> Juan J. Guerrero-González,<sup>e</sup> Ieda L.V. Rosa,<sup>b</sup> Manuel Algarra,<sup>f,g,\*</sup> Elson Longo<sup>b</sup>

<sup>a</sup> GNANO - Nanomedicine and Nanotoxicology Group, Physics Institute of São Carlos, University of São Paulo, 13566-590 São Carlos, SP, Brazil.

<sup>b</sup> CDMF - Center for the Development of Functional Materials, Federal University of São Carlos, 13565-905 São Carlos, SP, Brazil.

<sup>c</sup> IFSC - Physics Institute of São Carlos, University of São Paulo, São Carlos, SP, Brazil.

<sup>d</sup> SCAI - Central Service to Support Research Building (X-Ray Photoelectron Spectroscopy Lab.), University of Málaga. 29071 Málaga, Spain

<sup>e</sup> Policía Científica, Cuerpo Nacional de Policía, Málaga, Spain.

<sup>f</sup> Departamento de Ciencias, Universidad Pública de Navarra, Campus de Arrosadia, 31006 Pamplona, Spain.

<sup>g</sup> INAMAT<sup>2</sup>-Institute for Advanced Materials and Mathematics, Campus de Arrosadia 31006 Pamplona, Spain.

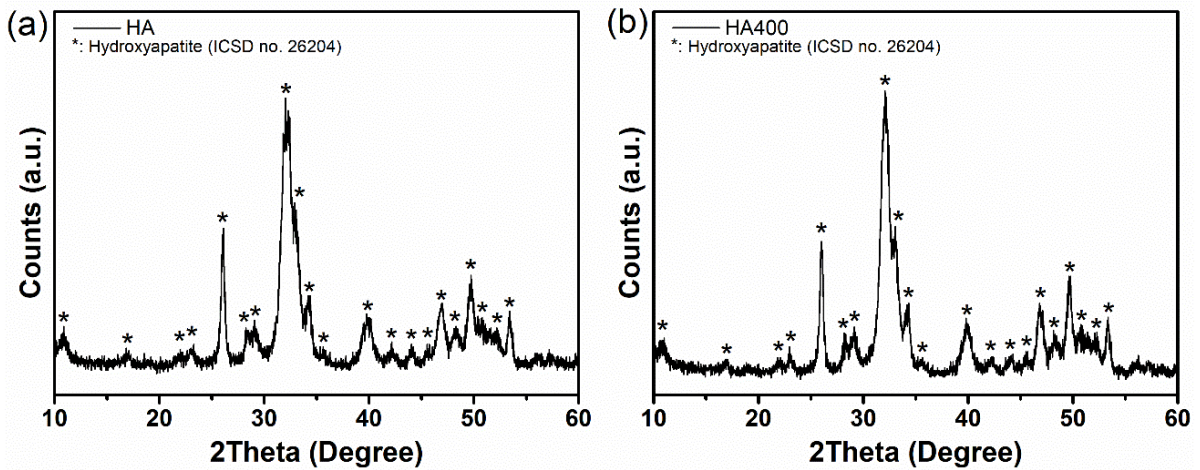


**Figure S1.** XRD patterns of (a) HA sample prepared by crystallization of ACP at 24h of reaction time, and (b) HA sample after heat treatment at 400 °C/4h.

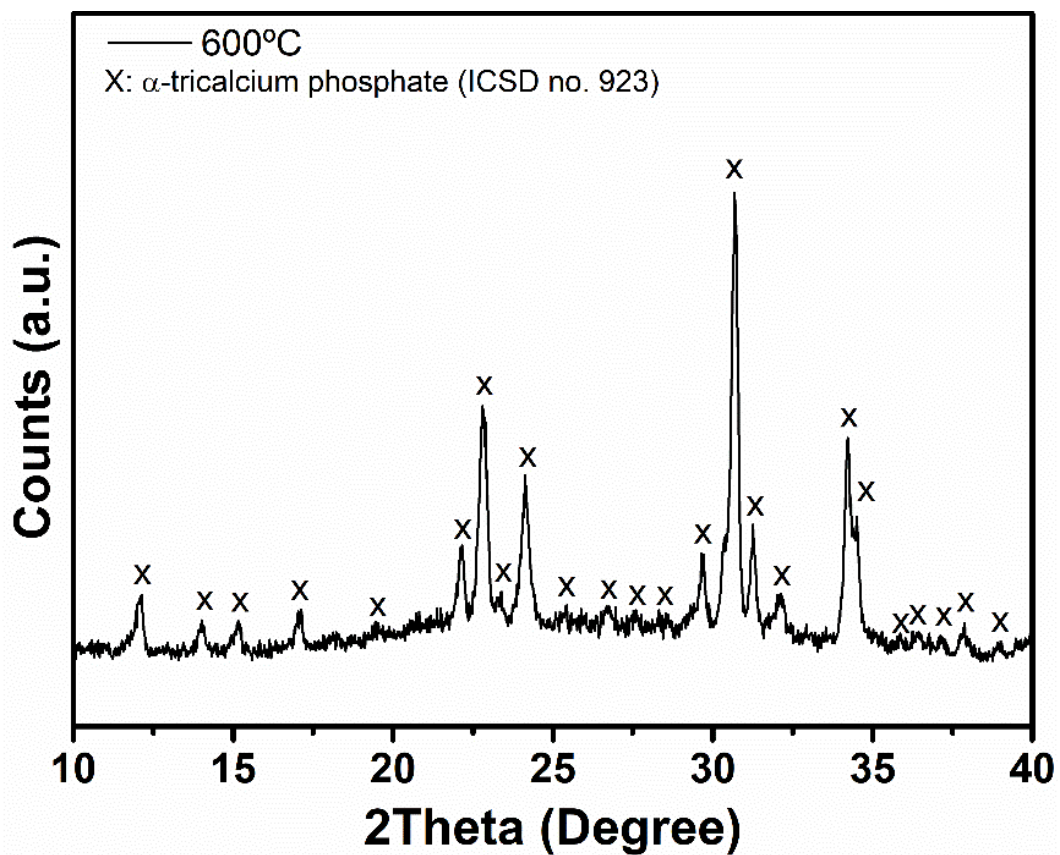


**Figure S2.** XRD pattern of ACP sample heat treated at 600 °C/4h.



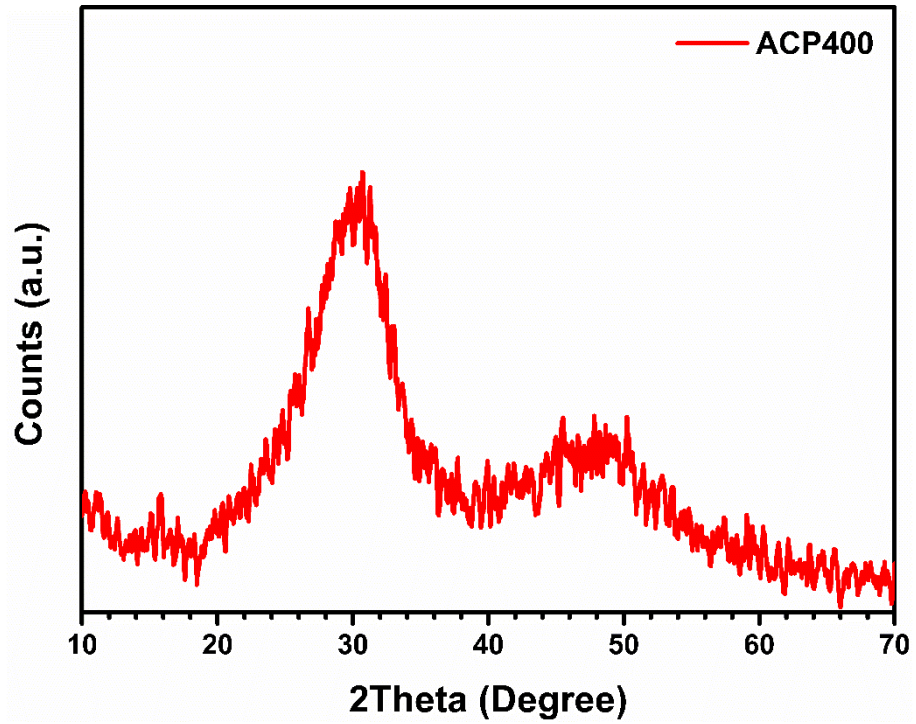


**Figure S3.** XRD pattern of ACP400 sample after the thermal aging treatment at 80 °C/8h.

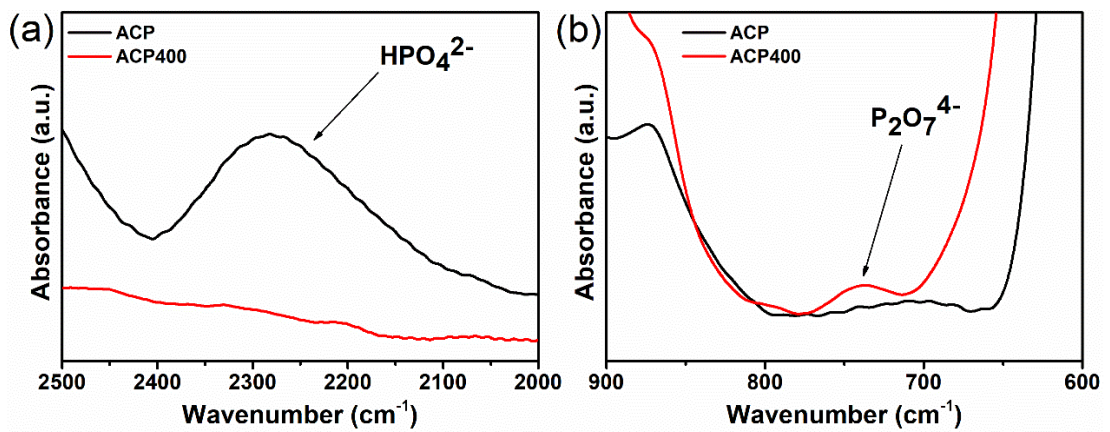


**Figure S4.** Magnified view of FTIR spectra on the region corresponding to the  $\text{HPO}_4^{2-}$  and  $\text{P}_2\text{O}_7^{4-}$  bands.

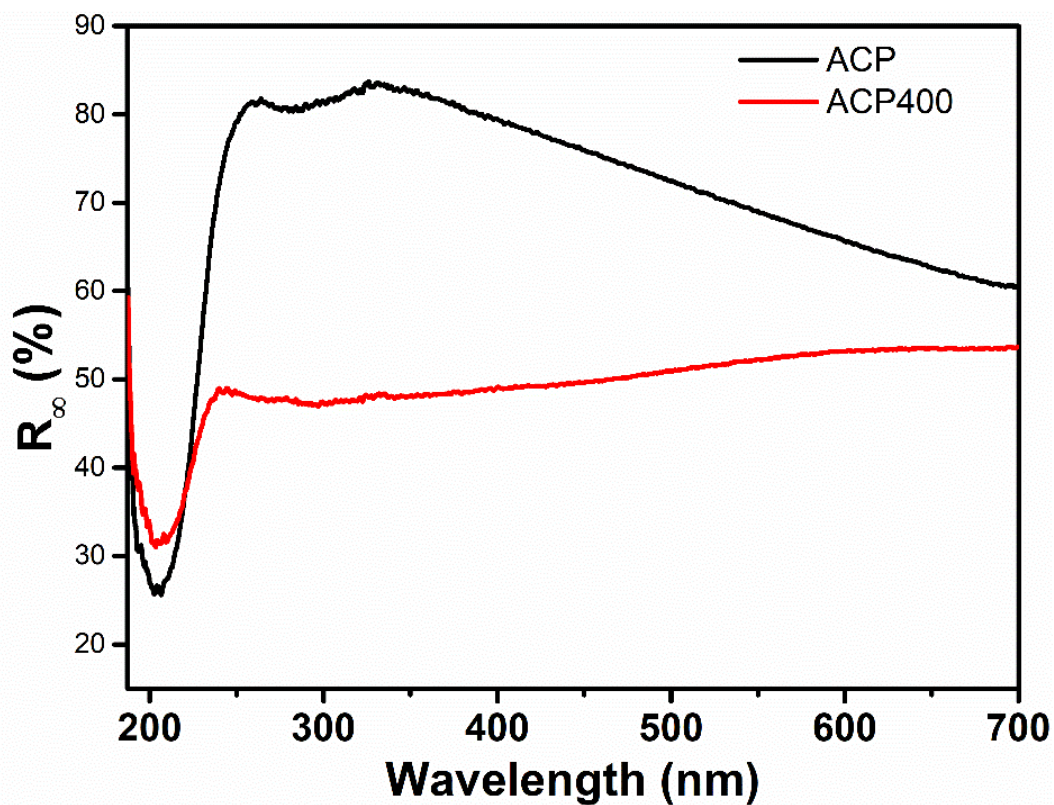


**Figure S5.** Diffuse reflectance spectrum of ACP and ACP400 NPs.

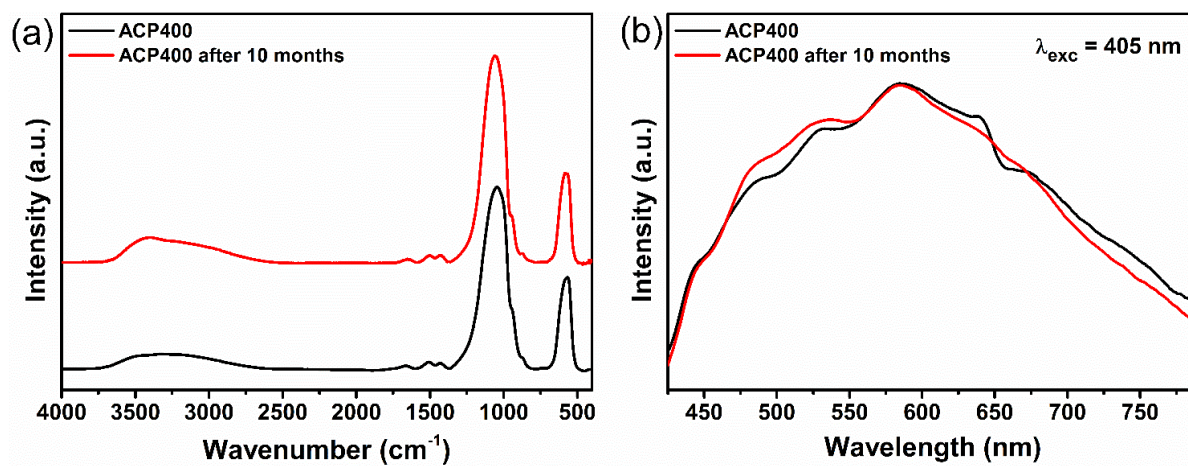


**Figure S6.** Stability analysis of ACP400 NPs. (a) FTIR, and (b) PL emission spectra.

## 5 – CONCLUSIONS

In this thesis, studies obtained during the doctorate were discussed, based on the high-impact article, which in addition to developing theories for the observed phenomena, associating the results of the techniques with data from the literature, also verified an effective application for the synthesized material.

The experiments were carried out in order to answer the following question: Is it possible to improve the luminescence of calcium orthophosphates without the addition of other elements, through simple synthesis, containing only the precursors of calcium and phosphate? That is, is it possible to enhance its intrinsic luminescence?

The results illustrate success for synthesis of intrinsically photoluminescent, biocompatible and stable nanoparticles based on chemically precipitated ACP and heat treated at 400°C for 4 hours. When excited at  $\lambda_{exc} = 450$  nm, the photoluminescence emission of heat-treated ACP nanoparticles is 50 times higher compared to freshly precipitated ACP and consists of an emission profile related to broadband defects centered at 540 nm and spanning most of the visible region (490 - 800nm).

Although the amorphous pattern is maintained after the heat treatment (verified by SAED, XRD), there is a significant decrease in the short-range structural ordering observed in FTIR. Such structural changes occur due to the shrinkage of the ACP network as an effect of the elimination of water of hydration at 400 °C. These phenomena, added to the vacancy formation of  $V_{Ca}$  and  $V_O$  in  $PO_4^{3-}$ , were attributed to possible causes of the high localized tail density and defect states in the forbidden band gap of the heat-treated ACP, detected by diffuse reflectance via UV-Vis spectroscopy, and by measurements of excitation and emission of photoluminescence.

The non-cytotoxic response of ACP observed by the MTT assay associated with its high luminescent intensity propelled us to the forensic application, thus treated ACP was used for fingerprint images, which revealed bright yellow patterns on the surface of tweezers and LCD smartphones under NUV irradiation ( $\lambda_{exc} = 450$  nm). The interactions of the nanoparticles with the fingerprint biomolecules revealed specific fluorescent patterns, with excellent contrast and sharpness for identification by IAFIS.

## 6 – REFERENCES

1. International Criminal Police Organization (INTERPOL). Retrieved from <<https://www.interpol.int/How-we-work/Forensics/Fingerprints>>. Accessed on September 5, 2022.
2. National Library of Medicine - National Institutes of Health. DNA Technology in Forensic Science. National Research Council (US), 1992. Retrieved from <<https://www.ncbi.nlm.nih.gov/books/NBK234540/>>. Accessed on September 5, 2022.
3. Swann, B. S; Libert, J. M.; Lepley, M. A.; Tools for quality control of fingerprint databases. BIOMETRIC TECHNOLOGY FOR HUMAN IDENTIFICATION VII, v. 7667 (766709), 2010. DOI:10.1117/12.850237
4. Landon, J. J. Federal Bureau of Investigation (FBI). Privacy Impact Assessment Integrated Automated Fingerprint Identification System (IAFIS)/Next Generation Identification (NGI) Biometric Interoperability., 2012. Retrieved from <<https://www.fbi.gov/services/information-management/foipa/privacy-impact-assessments/iafis-ngi-biometric-interoperability>>. Accessed on September 5, 2022.
5. Johnson E. C. From the inkpad to the mousepad IAFIS and fingerprint technology at the dawn of the 21st century Technical Bulletin. (2), 1998. Retrieved from <<https://www.ojp.gov/pdffiles1/Digitization/174917NCJRS.pdf>>. Accessed on September 5, 2022.
6. Zhang, R.; Wang, F. Research on Cogent Automatic Fingerprint Identification System. ADVANCED MATERIALS RESEARCH, v. 605-607, p. 1741–1747, 2013. DOI:10.4028/www.scientific.net/AMR.605-607.1741
7. Potcoava, M. C.; Kim, M. K. Fingerprint biometry applications of digital holography and low-coherence interferography. APPLIED OPTICS, v. 48(34), p. H9-H15, 2009. DOI:10.1364/AO.48.0000H9

8. Karu, K.; Jain, A. K. Fingerprint classification. *PATTERN RECOGNITION*. 29(3), 389–404. v. 29 (3), p. 389 404, 1996. DOI:10.1016/0031-3203(95)00106-9
9. Prabhakar, S.; Jain, A. K.; Pankanti, S. Learning fingerprint minutiae location and type. *PATTERN RECOGNITION*, v. 36(8), p. 1847–1857. 2003, DOI: 10.1016/s0031-3203(02)00322-9
10. Rajeev, S.; Kamath K. M. S.; Panetta, K.; Agaian, S. S. Forensic print extraction using 3D technology and its processing. *MOBILE MULTIMEDIA/IMAGE PROCESSING, SECURITY, AND APPLICATIONS 2017*, v. 10221 (UNSP 102210L), 2017. DOI: 10.1117/12.2262307
11. Chávez, D.; Garcia, C. R.; Oliva, J.; Diaz-Torres, L. A. A review of phosphorescent and fluorescent phosphors for fingerprint detection. *CERAMICS INTERNATIONAL*, v. 47(1), p. 10-41. 2020. DOI: 10.1016/j.ceramint.2020.08.259
12. Nicolodi, C.; Da Rosa, B. N.; Da Silva, C. C.; Berneira, L. M.; Pacheco, B. S.; Poletti, T; Venzke, D.; Mariotti, K. C.; Pereira, C. M. P. Application of pieces on the development of latent fingermarks an experiment in chemistry teaching. *QUÍMICA NOVA*, v. 42 (8), p. 962-970, 2019. DOI: 10.21577/01004042.20170405
13. González, M.; Gorziza, R. P.; Mariotti, K. C.; Limberger, R. P. Methodologies Applied to Fingerprint Analysis\*. *JOURNAL OF FORENSIC SCIENCES*, v. 65 (4), p. 1040–1048, 2020. DOI:10.1111/1556-4029.14313
14. Haan, P. V. Physics and fingerprints. *CONTEMPORARY PHYSICS*, v. 47(4), p 209–230, 2006. DOI:10.1080/00107510600893986
15. G.S. Sodhi; J. Kaur. Powder method for detecting latent fingerprints: a review. *FORENSIC SCIENCE INTERNATIONAL*, v. 120(3), p. 172–176, 2001. DOI: 10.1016/s0379-0738(00)00465-5

16. Machado, T.R. Study, characterization and properties of multifunctional orthophosphates. São Carlos, São Paulo - Brazil, Postgraduate Program in Chemistry - Federal University of São Carlos, 2016. THESIS, 195 p
17. Edinburgh Instruments. What is the Difference between Luminescence, Photoluminescence, Fluorescence, and Phosphorescence? Retrieved from<<https://www.edinst.com/blog/photoluminescence-differences/>>. Accessed on September 5, 2022.
18. Wang, M.; Li, M.; Yu, A.; Wu, J.; Mao, C. Rare Earth Fluorescent Nanomaterials for Enhanced Development of Latent Fingerprints. ACS APPLIED MATERIALS & INTERFACES, v. 7(51), p.28110-28115, 2015. DOI:10.1021/acsami.5b09320
19. Park, S. J.; Park, J. Y.; Yang, H. K.. Luminescence of a novel cyan emitting  $\text{Sr}_{10}(\text{PO}_4)_6\text{O}:\text{Ce}^{3+}$  phosphor for visualization of latent fingerprints and anti-counterfeiting applications. SENSORS AND ACTUATORS B: CHEMICAL, v. 262, p. 542–554, 2018. DOI:10.1016/j.snb.2018.02.053
20. Hong, W. T.; Park, J. Y.; Je, J.; Yang, H. K. Sintering temperature effect of divalent europium ion doped tetra-calcium phosphate phosphors for latent fingerprint detection. OPTICAL MATERIALS, v. 81, p. 37–44, 2018. DOI:10.1016/j.optmat.2018.05.017
21. Pushendra; Suryawanshi, I; Kalia, R.; Kunchala, R. K.; Mudavath, S. L.; Naidu, B. S. Detection of latent fingerprints using luminescent  $\text{Gd}_{0.95}\text{Eu}_{0.05}\text{PO}_4$  nanorods. JOURNAL OF RARE EARTHS, v. 40(4), p. 572–578, 2022, DOI: 10.1016/j.jre.2021.01.015
22. Neto, A. S.; Ferreira, J. M. F. Synthetic and Marine-Derived Porous Scaffolds for Bone Tissue Engineering. MATERIALS, v. 11(9), p. 1702, 2018. DOI:10.3390/ma11091702
23. Götze, J; Heimann, R. B.; Hildebrandt, H.; Gburek, U. Microstructural investigation into calcium phosphate biomaterials by spatially resolved cathodoluminescence. MATERIALWISSENSCHAFT UND WERKSTOFFTECHNIK, v. 32(2), p 130–136, 2001. DOI:10.1002/1521-4052(200102)32:2<130::aid-mawe130>3.0.co;2-z

24. Aronov, D.; Chaikina, M.; Haddad, J.; Karlov, A.; Mezinskis, G.; Oster, L. Pavlovska, I.; Rosenman, G. Electronic states spectroscopy of Hydroxyapatite ceramics. *JOURNAL OF MATERIALS SCIENCE-MATERIALS IN MEDICINE*, v. 18, p. 865–870, 2007. DOI: 10.1007/s10856-006-0080-3.
25. Machado, T.R.; Sczancoski, J.C.; Beltrán-Mir, H.; Nogueira, I.C.; Li, M.S.; Andrés, J. Cordoncillo, E.; Longo, E. A novel approach to obtain highly intense self-activated photoluminescence emissions in hydroxyapatite nanoparticles. *JOURNAL OF SOLID STATE CHEMISTRY* . v. 249, p. 64–69, 2017. DOI: 10.1016/j.jssc.2016.12.018.
26. Machado, T.R.; Sczancoski, J.C.; Beltrán-Mir, H.; Li, M.S.; Andrés, J. Cordoncillo, E.; Leite, E.; Longo, E. Structural properties and self-activated photoluminescence emissions in hydroxyapatite with distinct particle shapes. *CERAMICS INTERNATIONAL*, v. 44, p. 236–245, 2018. DOI: 10.1016/j.ceramint.2017.09.164.
27. Hoeher, A. J. Chemical Controls on the Formation of Amorphous and Crystalline Calcium Phosphates. Blacksburg, Virginia - EUA, Department Geosciences - Virginia Polytechnic Institute and State University, 2020. DISSERTATION, 98 p.
28. Roohani, I.; Cheong, S.; Wang, A. How to build a bone? - Hydroxyapatite or Posner's clusters as bone minerals. *OPEN CERAMICS*, v. 6 2021. DOI: 10.1016/j.oceram.2021.100092
29. Stammeier, J. A.; Purgstaller, B.; Hippler, D.; Mavromatis, V.; Dietzel, M. In-situ Raman Spectroscopy of Amorphous Calcium Phosphate to Crystalline Hydroxyapatite Transformation. *METHODSX*, v. 5, p. 1241-1250, 2018. DOI:10.1016/j.mex.2018.09.015
30. Du, L.W.; Bian, S.; Di Gou, B.; Jiang, Y.; Huang, J.; Gao, Y.X.; Zhao, Y.D.; Wen, W.; Zhang, T. L.; Wang, K. Structure of clusters and formation of amorphous calcium phosphate and hydroxyapatite: From the perspective of coordination chemistry. *CRYSTAL GROWTH & DESIGN*, v. 13, p. 3103–3109, 2013. DOI: 10.1021/cg400498j.